Validation of Models for Net Deployment and Capture Simulation with Experimental Data

Achira Boonrath* and Eleonora M. Botta†
University at Buffalo, Buffalo, New York 14260

https://doi.org/10.2514/1.A35798

This work validates lumped-parameter models and cable-based models for nets against data from a parabolic flight experiment. The capabilities of a simulator based in Vortex Studio, a multibody dynamics simulation framework, are expanded by introducing i) a lumped-parameter model of the net with lumped masses placed along the threads and ii) a flexible-cable-based model, both of which enable collision detection with thin bodies. An experimental scenario is recreated in simulation, and the deployment and capture phases are analyzed. Good agreement with experiments is observed in both phases, although with differences primarily due to imperfect knowledge of experimental initial conditions. It is demonstrated that both a lumped-parameter model with inner nodes and a cable-based model can enable the detection of collisions between the net and thin geometries of the target. While both models improve notably capture realism compared to a lumped parameter model with no inner nodes, the cable-based model is found to be most computationally efficient. The effect of modeling thread-to-thread collisions (i.e., collisions among parts of the net) is analyzed and determined to be negligible during deployment and initial target wrapping. The results of this work validate the models and increase the confidence in the practicality of this simulator as a tool for research on net-based capture of debris. A cable-based model is validated for the first time in the literature.

Nomenclature

A_{cross}	=	cross-sectional area of a thread, m^2
$\boldsymbol{a}$	=	absolute acceleration, m/s^2
$\boldsymbol{C}$	=	connectivity matrix
c_a	=	axial damping coefficient of a thread section, N·s/m
$\bar{c}$	=	linear axial damping of a thread section, N · s
d_e	=	head diameter of the experimental truncated-cone-shaped canister, m
E	=	Young's modulus, Pa
$\boldsymbol{e}$	=	axial unit vector of a section of a thread of the net
$\boldsymbol{F}_{\text{ext},s}$	=	each of the S_i external forces on a node, N
$\boldsymbol{F}_{\text{par}}$	=	forces on a node from the parabolic flight environment, N
$\boldsymbol{g}_r$	=	parabolic flight residual gravity, m/s^2
h_{panel}	=	thickness of the solar panel model, m
I_{CM}	=	set of four numbers corresponding to the indices assigned to the corner masses
$\hat{\boldsymbol{i}}, \hat{\boldsymbol{j}}, \hat{\boldsymbol{k}}$	=	inertial reference frame
J	=	capture quality index
k_a	=	axial stiffness coefficient of a thread section, N/m
$\bar{k}$	=	linear axial stiffness of a thread section, N
L_c	=	shortest distance between the centroid of the target and its surface, m
L_{side}	=	net side length, m
l, l_{ct}, l_{net}	=	length of a thread section, of a corner thread, and of a mesh, m
$l_{\min}$	=	minimum distance used for number of corner nodes computation, m
m	=	mass, kg
N_{ct}, N_I	=	number of inner nodes per corner thread and per inner thread
$N_{I,\text{base}}$	=	baseline number of inner nodes for the validation effort
$N_{I,S}$, $N_{\text{ct},S}$	=	smallest number of inner nodes per corner thread and per inner thread for a realistic capture
$N_{\text{present}}(t)$	=	number of nodes for which experimental data are available at time t
N_s	=	number of knots on each side of the net proper
n_{sec}	=	number of sections per cable-based thread
q_n	=	distance between the centroids of the net and of the target, m
$\text{RMSE}_{\text{mean}}$	=	mean root-mean-square error between experimental net and simulated net, m
$\text{RMSE}(t)$	=	root-mean-square error between experimental net and simulated net at time t, m
r	=	thread radius, m
$\boldsymbol{r}$	=	inertial position, m
$\boldsymbol{re}$	=	residual error, m
S	=	convex hull surface area, m^2
$\boldsymbol{T}$	=	tension force, N
V	=	convex hull volume, m^3
$\boldsymbol{v}$	=	velocity, m/s
v_e	=	ejection speed, m/s
v_r	=	magnitude of relative velocity between two adjacent nodes, m/s
$x^E(t), y^E(t), z^E(t)$	=	coordinates of an experimental position at time t
$x^S(t), y^S(t), z^S(t)$	=	coordinates of a simulated position of at time t
α	=	stowing ratio of the net (between 0 and 1)
θ	=	ejection angle from the overall direction of deployment, deg
$\bar{\rho}$	=	linear density, kg/m
$\boldsymbol{\omega}_r$	=	parabolic flight residual angular acceleration, rad/s^2

Subscripts

CM	=	corner mass
ct	=	corner thread
i	=	index for a node of the net

Presented as Paper 2022-1773 at the AIAA SciTech 2022 Forum, San Diego, CA, & Virtual, January 3–7, 2022; received 8 June 2023; revision received 25 July 2023; accepted for publication 28 July 2023; published online 25 August 2023.

*Ph.D. Student, Department of Mechanical and Aerospace Engineering, Student Member AIAA.

†Assistant Professor, Department of Mechanical and Aerospace Engineering; ebotta@buffalo.edu. Member AIAA (Corresponding Author).

k	=	index for a thread section
knot	=	physical knot of the net
n	=	convex hull properties of the net
net	=	physical quantities of the net proper's interior
perimeter	=	physical quantities of the net proper's perimeter
t	=	convex hull properties of the target
x, y, z	=	components of a vector in the inertial frame
0	=	unstretched condition

I. Introduction

THE increase in the number of debris objects in low Earth orbit causes significant challenges to daily spacecraft operations and threats to the future use of these orbits. Therefore, there is currently a need for technologies capable of safely and efficiently removing debris from orbit. Among uncontrolled objects in orbit, large pieces of debris are particularly problematic, as their collision with other objects can lead to powerful fragmentation and the creation of more pieces of debris on several different orbits, as was seen when Cosmos 2251 and Iridium 33 collided in 2009 [1]. Based on these premises, a number of Earth-orbiting objects have been identified as priority targets for debris removal missions, including the satellite Envisat and multiple second stages from Zenit-2 launchers [2,3].

Among the proposed technologies for active debris removal (ADR), tether-nets are regarded as particularly promising, especially for the removal of large and massive objects such as defunct satellites and launcher upper stages, given that they are lightweight, can be packaged in a small volume, are versatile with respect to the configuration and rotational state of the target, and allow the chaser spacecraft to remain at a safe distance [4–6]. Because of the low-medium technological readiness of tether-net systems for use in space, it is necessary that the dynamics of nets in space is thoroughly studied and clearly understood through simulation and analysis, before actual net-based debris removal missions can be pursued. To this aim, simulators of the deployment and capture dynamics of tether-nets in space have been implemented by Benvenuto et al. [7], Medina et al. [8], Botta et al. [5,9,10], Shan et al. [11,12], and more recently by Si et al. [13], Endo et al. [14], Huang et al. [15,16], and Hou et al. [17]. Numerous studies on the deployment and capture dynamics have been performed thanks to these tools [7,18–23]. Recently, Zhang et al. [24] and Shan and Shi [25] have proposed simplified net models intended to lower the computational cost of simulation, although for the deployment phase only.

The validation of simulators against real-world data is a fundamental step to ensure their accuracy and capability of providing meaningful insight into tether-net dynamics. Previous efforts to validate the standard lumped-parameter (LP) model of the net include comparison to experimental data collected in a drop test under gravity [22]. Because of the microgravity conditions in which these systems are meant to operate, parabolic flight experiments were conducted by Medina et al. [8] and Gołębiowski et al. [26] in collaboration with the European Space Agency. In these experiments, a net was used to capture a scaled-down model of Envisat in microgravity conditions. Medina et al. used such data to validate their simulator, based on a LP model of the net [8]. The second set of data was employed to validate simulators by Gołębiowski et al. [26] and Shan et al. [11]: Gołębiowski et al. [26] validated a Cosserat-rod-based net model in deployment and capture qualitatively, showing similarities in the shapes of the simulated and experimental nets; Shan et al. validated an LP-based and an absolute nodal coordinate formulation (ANCF)-based simulation models in net deployment only [11]. Previous work by the authors employed data from the parabolic flight experiment in [26] for the validation of the deployment dynamics only, and limited to a model of the net where the mass is simply lumped at the physical knots of then net [27]. A preliminary validation effort including the capture phase was performed only recently [28] and is expanded upon in this work.

The aim of the work discussed in this paper is to validate and analyze the performance of simulation models based on i) a dense mesh of LP elements and ii) flexible *cable-based* modeling for the net, and of continuous-compliant modeling for contact dynamics. While some of these models and the relative implementation in simulation were developed by Botta et al. in previous work [5,9,10], several limitations of the models are addressed here. Compared to the preliminary validation work in [28], the LP model has been improved, and a flexible cable-based model for the net has been introduced, both of which allow for increased realism, especially during the capture phase. Results of simulation of both the deployment and capture phases with i) LP modeling with a varying number of inner nodes and ii) cable-based modeling are analyzed and compared to data from the parabolic flight experiment by Gołębiowski et al. [26].

As a result of this work, a simulation tool for the dynamics of net deployment and target capture, implemented in the multibody dynamics software Vortex Studio, is validated against experimental data. Throughout the work, the effect of the inclusion of inner nodes on the similarity between simulated and experimental data is analyzed. The capability of the simulator to include 20 inner nodes per thread is demonstrated, as well as the simulator's ability to replicate the wrapping of thin target geometries. It is demonstrated that the inclusion of a higher number of inner nodes improves simulation fitness to reality. The effect of disabling node-to-node and cable-to-cable contact (i.e., the contact of the net with itself) on target capture dynamics is analyzed. Finally, a cable-based model of the net is validated here for the first time in the literature.

This paper is organized as follows. In Sec. II, the LP model with inner nodes and the cable-based model are introduced. Section III briefly details the parabolic flight experiment and discusses general aspects of the simulation, including the recreation of the experimental conditions in simulation, the determination of the minimum number of inner nodes required for a realistic capture simulation, the determination of initial conditions, and considerations on collision detection. Section IV presents the validation results, including the calculation of errors between simulations and the experiment, visualization of the experimental and simulated nets, an exploration of the effect of including inner nodes on the accuracy and computational cost of the simulation, and the analysis of the effect of representing thread-to-thread collisions. Section V concludes the paper with final remarks.

II. Modeling of the Net

A widespread design for nets to be used for the purpose of debris removal is characterized by a net with a square planar geometry and four corner masses, each attached via a thread to a corner of the net [5,7] (see Fig. 1a). Hexagonal, conical, and pyramidal nets have also been studied in simulations [7,15–17,24,29], and a hemispherical net was utilized in the RemoveDEBRIS in-orbit demonstration mission [30,31]. However, in the experiment by Gołębiowski et al. [26] the net was square, with four cylindrical "bullets" attached to its four corners; therefore, in the rest of this work, focus will be on such geometry.

The most common method for modeling these nets is the standard LP model [5,11,21,32–35], which was also used previously for fishing nets, with the main difference being the inclusion of buoyancy and hydrodynamic forces from water on the threads [36–38]. Similar in principle to the LP-model with inner nodes to be validated in this work, Lee et al., Benvenuto et al., and Shan et al. [7,38,39] augmented the standard LP model through the inclusion of lumped masses along the threads of the net. Additionally, Botta et al. investigated the effects of bending stiffness for modeling space tether-net systems, and found that, whereas the inclusion of bending stiffness does have a noticeable effect on the dynamics, the overall result of debris capture is the same whether bending stiffness is implemented within the simulation or not [9]. Alternative modeling approaches that have been employed to represent the dynamics of the net include the ANCF [11], Cosserat rods [26], and discrete elastic rods [15–17]. In the remainder of this section, two models of the dynamics of the net are presented, which will be validated in this work. Both models are available in the Vortex Studio–based simulator subject of this and previous work [5,9,10].

A. Lumped-Parameter Model of the Net with Inner Nodes

The LP model lumps the mass of the physical net into particles (herein called *nodes*) and assumes that the threads are massless

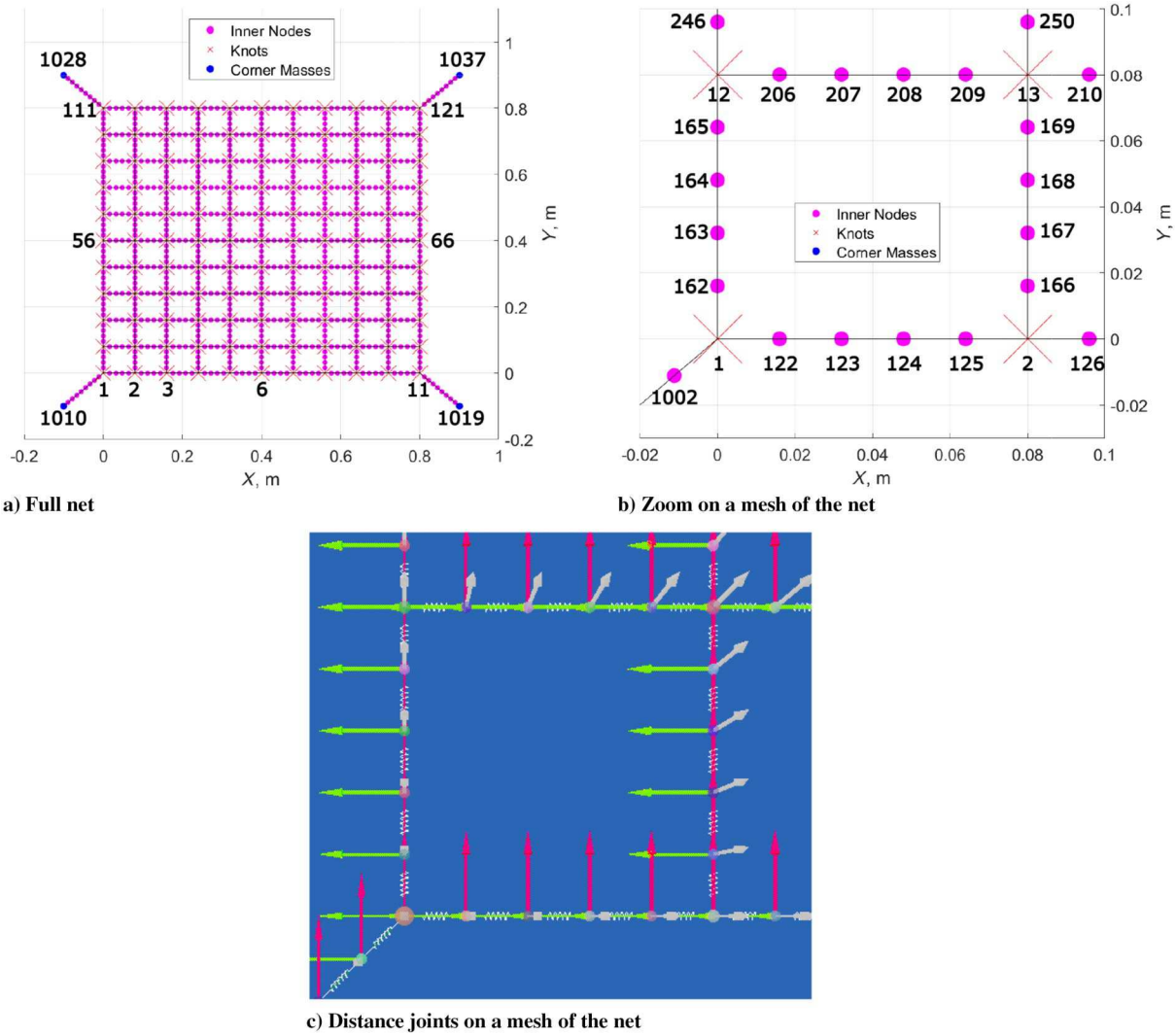

a) Full net

b) Zoom on a mesh of the net

c) Distance joints on a mesh of the net

Fig. 1 Model of a net with inner nodes: visualization of knots, corner masses, inner nodes, and distance joints for a net with $N_s = 11$, $N_I = 4$, and $N_{ct} = 9$.

Kelvin–Voigt elements that cannot withstand compression. In the standard LP model, the nodes include the physical knots of the net and the four corner masses, and each thread of the net is represented with a massless spring and a damper placed in parallel. Because Vortex Studio is a multibody dynamics simulation framework in which any body is a rigid body, the nodes of the net are actually modeled as small spherical bodies, which are linked together by relaxed *distance joints* that are active when the distance between adjacent nodes is larger than a certain unstretched thread length. The distance joints represent the Kelvin–Voigt elements with no compression resistance [5,9].

In previous work, it was verified that if the nodes of the LP model are only placed at the physical knots of the net, then the dynamics of capturing thin targets—that is, targets with one or more physical dimensions that are smaller than the mesh length of the net—is unphysical [5]. In fact, collision detection cannot be performed along the threads of the net, where there is no mass. To enable proper collision detection and contact dynamics of the net with thin targets, the simulator at hand possesses the capability to model the threads of the net with N_I additional nodes (called *inner nodes* and represented as additional small rigid bodies) per thread and with additional joints, if desired. The portion of a thread among two adjacent nodes is then modeled with a distance joint, and a thread of the net is therefore modeled as a series of small spherical rigid bodies and distance joints. In addition to enabling improvements upon the collision detection ability of the net model, the LP model with inner nodes is expected to ensure more realistic mass distribution. Introduction of inner nodes, however, comes at the cost of much increased computational time. For visualization of the geometry and modeling of the net, Fig. 1a shows a sample net with $N_s = 11$, $N_I = 4$, and $N_{ct} = 9$. Figure 1b depicts an enlargement of the first mesh of the net, and Fig. 1c depicts distance joints within Vortex Studio on the same mesh of the net (where the green, gray, and red arrows represent the body frame of each node of the net, and the springs represent the distance joints).

A square net with square mesh and N_s knots on a side is composed of N_s^2 knots, where a knot is a node on the net proper that acts as a connection point for the physical threads of the net. For the purposes of node identification and creation of a connectivity table, each node of the net is assigned an index. The numbering of nodes is reported in Figs. 1a and 1b for the sample net with $N_s = 11$ and $N_I = 4$. First, the knots of the net are numbered from 1 to $N_s^2 = 121$ starting from the node initially located at the coordinate origin of the chosen reference frame (see Figs. 1a and 1b). Then, the inner nodes of the net are assigned indices from $N_s^2 + 1 = 122$ to $N = N_s^2 + 2N_s(N_s - 1)N_I = 1001$, starting from the inner node that is nearest to node 1 on the positive x axis. Once all of the inner nodes are numbered, nodes located on the corner threads are assigned indices from $N + 1 = N_s^2 + 2N_s(N_s - 1)N_I + 1 = 1002$ to $N_s^2 + 2N_s(N_s - 1)N_I + 4N_{ct} = 1037$, starting from the corner thread that is connected to node 1.

To store information regarding how the nodes are connected to each other for the net proper, matrix $\boldsymbol{C}$ is created based on the above indices. The matrix has dimensions of $N_s + N_I(N_s - 1)$ by $N_s + N_I(N_s - 1)$. Equation (1) provides an example where $\boldsymbol{C}$ is constructed with $N_I = 4$ and $N_s = 11$, and the matrix has dimensions of 51 by 51. Each element

of the matrix is the index of a node, and the location of each entry in the matrix indicates the placement of that node relative to adjacent nodes in the net. Accordingly, for example, node 1 is located at a corner of the net and is adjacent to node 122 and node 162.

The entries of $\boldsymbol{C}$ are filled starting with the first row of the matrix, which possesses both knots and inner nodes. The knots of the net are assigned first to the matrix, with vacant entries located between the knot entries. After all the knots are assigned, the inner nodes are then filled into $\boldsymbol{C}$. The inner nodes are inserted in a manner such that the knots are linked together to form a square mesh pattern. Rows with both knots and inner nodes are found every other $N_I + 1$ rows of the matrix. On the rows in which knots are absent, values of zero are assigned in place of inner nodes, to represent gaps between threads of the net. Once this construction completed, $\boldsymbol{C}$ is a square matrix representative of the geometry of the net proper [see the example in Eq. (1)].

$$\boldsymbol{C} = \begin{bmatrix} 1 & 122 & 123 & 124 & 125 & 2 & 126 & \cdots & 11 \\ 162 & 0 & 0 & 0 & 0 & 166 & 0 & \cdots & 202 \\ 163 & 0 & 0 & 0 & 0 & 167 & 0 & \cdots & 203 \\ 164 & 0 & 0 & 0 & 0 & 168 & 0 & \cdots & 204 \\ 165 & 0 & 0 & 0 & 0 & 169 & 0 & \cdots & 205 \\ 12 & 206 & 207 & 208 & 209 & 13 & 210 & \cdots & 22 \\ \vdots & \vdots & \vdots & \vdots & \vdots & \vdots & \vdots & \ddots & \vdots \\ 111 & 962 & 963 & 964 & 965 & 112 & 966 & \cdots & 121 \end{bmatrix} \tag{1}$$

For the purpose of thread assignment, the matrix can be manipulated into a connectivity table such as what is shown in Table 1, which indicates that the kth thread section connects node i and node j; for example, thread 1 connects node 1 and node 122, thread 2 connects node 1 and node 162, etc. The connectivity table is first constructed for the net proper. Afterward, connectivity information of the nodes on the corner threads is appended to the table: the first node of each corner thread is connected to a node on the corner of the net proper; then, the subsequent nodes on each corner thread are connected in series up to the corner masses.

With the connectivity information defined, the equation of motion can be written for each node of the net, as

$$m_i \boldsymbol{a}_i = \sum_{k \in K_i} \pm \boldsymbol{T}_k + \sum_{s=1}^{S_i} \boldsymbol{F}_{\text{ext},s,i} \tag{2}$$

where $\boldsymbol{T}_k$ is each of the tension forces in the threads adjacent to the ith node (belonging to the set K_i, as per the connectivity table), and $\boldsymbol{F}_{\text{ext},s,i}$ is each of the S_i external forces on the ith mass. If m_k, m_{knot}, and m_{CM} represent the mass of the kth thread section of the net, the mass of an individual physical knot, and the mass of an individual corner mass, respectively, then the mass of the ith node of the net can be calculated as

$$m_i = \begin{cases} \sum_{k \in K_i} \dfrac{m_k}{2} + m_{\text{knot}} & 1 \le i \le N_s^2 \\ \sum_{k \in K_i} \dfrac{m_k}{2} & i > N_s^2, i \notin I_{\text{CM}} \\ \sum_{k \in K_i} \dfrac{m_k}{2} + m_{\text{CM}} & i \in I_{\text{CM}} \end{cases} \tag{3}$$

Table 1 Connectivity table example

Thread k:	1	2	3	4	5	6	7	⋯
Node i:	1	1	122	123	124	125	2	⋯
Node j:	122	162	123	124	125	2	126	⋯

where the first row indicates the knots of the net, the second indicates the inner nodes, and the third indicates the corner masses; in the example in Fig. 1, $I_{\text{CM}} = \{1010,1019,1028,1037\}$. Meanwhile, the tension force in the kth thread section of the net is modeled as

$$\boldsymbol{T}_k = \begin{cases} T_k \boldsymbol{e}_k & \text{if } (l_k > l_{k,0}) \\ \boldsymbol{0} & \text{if } (l_k \le l_{k,0}) \end{cases} \tag{4}$$

where $T_k = k_{a,k}(l_k - l_{k,0}) + c_{a,k} v_{r,k}$. It is worth noting that, when $N_I = 0$, this model is equivalent to the standard LP model.

The external forces term $\boldsymbol{F}_{\text{ext},s,i}$ in Eq. (2) collects all forces acting on the ith node other than tension, including contact forces. In general, collisions can happen both between the nodes of the net and the surface of the target, and among the nodes of the net. For the purpose of contact modeling, each node is given a small spherical collision geometry with a radius proportional to its mass [5,9], and collision geometries composed of patched primitives are used to model the target (see Sec. III.A). In each time step of the simulation, collision geometries are checked for intersection with others. Normal contact forces are computed by describing the contact dynamics as happening in a finite amount of time through a continuous compliant model [5,9,40], whereas friction forces are determined in accordance with an approximated Coulomb's friction model. Previous works by Botta et al. [5,9,20] are recommended for readers interested in additional information concerning contact dynamics of net-based debris capture.

B. Cable-Based Model of the Net

An alternative modeling approach that allows for collision detection of the net with thin geometries of a target object is what is referred here as *cable-based* modeling. With the cable-based model, each thread in the net is represented by a flexible cable consisting of a sequence of slender capsule-like rigid bodies (herein referred to as *sections* of a cable) linked together via prismatic constraints [5,10]. The cables link together either two physical knots of the net or a physical knot and a corner mass. Hence, the mass of the threads and corner threads is distributed along the cables, rather than being lumped in the nodes as in the LP model. Here, the length of the cable and the density of its material are taken to be the same as the given thread of the experimental net. Nodes, still in the form of spherical rigid bodies, remain employed to represent the physical knots of the net and corner masses. As defined in Sec. II.A, the knots of the net have a mass of m_{knot}, while the corner masses have a mass of m_{CM}. The computation of contact forces on each cable section is done using the same formulation as that of the nodes of the net [5].

In principle, the relaxed prismatic constraints that are placed between any two sections of a cable allow modeling the axial, bending, and torsional stiffness and damping of the threads. For this validation work—similarly to what is done with the LP modeling—bending and torsional resistance to deformation are set to be negligible.[‡] Using n_{sec} sections (i.e., n_{sec} rigid bodies) in a cable introduces $n_{\text{sec}} - 1$ prismatic joints; this results in a flexible portion of the cable that is $(n_{\text{sec}} - 1)/n_{\text{sec}}$ times the total length of the cable [5]. A close-up diagram of cable sections can be seen in Fig. 2, which showcases a cable composed of three sections and two prismatic joints, and the red parts indicate nonflexible segments. To match the axial stiffness and damping properties of each cable, the following is set:

$$(EA_{\text{cross}})_{\text{cable}} = EA_{\text{cross}} \left(\frac{n_{\text{sec}} - 1}{n_{\text{sec}}} \right) \tag{5}$$

In the only prior work employing cable-based modeling of a net, a small net with four sections ($n_{\text{sec}} = 4$) for each thread was simulated, due to computational difficulties in simulating a large number of rigid bodies [5]. With improvements to the simulator, it is now possible to use six sections ($n_{\text{sec}} = 6$) for each thread of the net. As such, for this

[‡]In practice, this is achieved by setting the bending stiffness coefficient and the bending damping coefficient of the prismatic constraints to very small numbers, and disabling torsional resistance entirely.

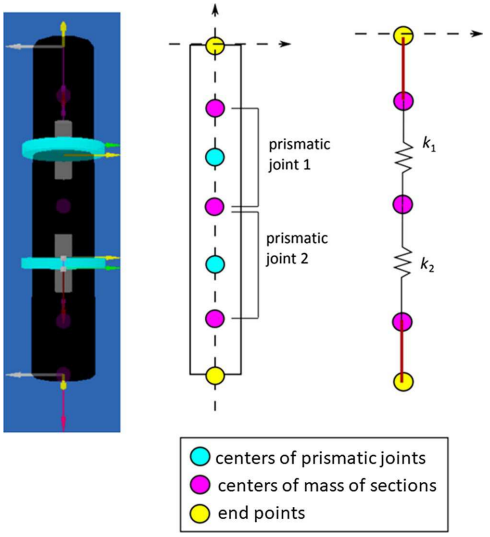

Fig. 2 Close-up diagram of a three-section cable [5].

validation work, the simulation results from the cable based with $n_{sec} = 6$ will be utilized, as the higher number of sections better reflects the nature of the physical threads, which can bend at any location along their length.

III. Parabolic Flight Experiment and Simulation Setup

Data regarding the deployment of a scaled-down net and capture of a correspondingly scaled Envisat satellite model onboard a parabolic flight are employed for validation of the simulator. Although the experiment performed by Gołębiowski et al. consisted of multiple net launches and captures of the target mock-up [26], here data from a single experiment are employed, which are available to the authors. The net used in the experiment was shot by means of a pneumatic launcher toward the scaled-down Envisat satellite model, 1/25th the size of the actual satellite. The mock-up target was supported by a metal arm, placed at the side of the target opposite to the net launcher [26]. Four cameras were employed to record the net deployment and target capture, and images were postprocessed to reconstruct the position of the nodes of the net [26]. In the experiment instance available to the authors, the net took approximately 0.91 s to travel from the launcher to the target, and the capture of the target was recorded between approximately 0.91 and 5.5 s after the net was launched. The rest of this section discusses considerations related to the parabolic flight experiment and how they impact the simulation setup.

A. Model of the Target

The scaled-down model of the Envisat satellite is represented in simulation with a collection of cylinders and rectangular prisms of dimensions matching those specified for the experimental target. Figure 3 shows the collision geometry of the target in the Vortex Studio Editor, where the direction of launch of the net goes into the page. In terms of dynamics, because the mock-up target was rigidly attached to the airplane, the target is assumed to be fixed in the reference frame of the simulation.

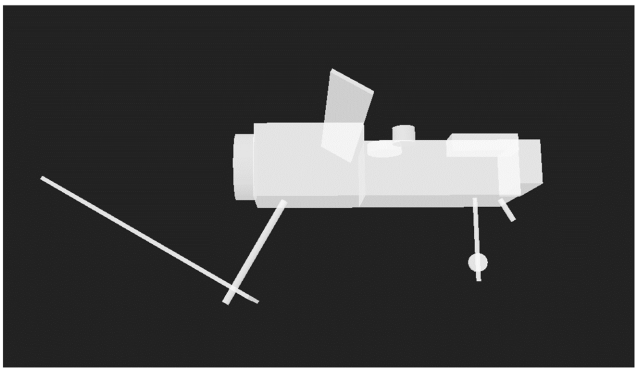

Fig. 3 Scale model of Envisat as recreated in the simulator [28].

B. Physical Properties of the Net

The physical properties of the simulated net and of its corner masses were selected to match those from the experimental net, and are compiled in Table 2. From the values of the side length of the net L_{side} and of the unstretched mesh length of the net $l_{net,0}$, it is clear that the net used in the parabolic flight experiment has 11 physical knots on a side of the net (i.e., $N_s = 11$). Also, it is noted that the perimeter of the net is made of thicker threads (of radius $r_{perimeter}$), compared to the rest of the net (made of threads of radius r_{net}); this entails different linear densities ($\bar{\rho}_{perimeter}$ and $\bar{\rho}_{net}$), axial stiffness constants per unit length ($\bar{k}_{perimeter}$ and $\bar{k}_{net}$), and axial damping constants per unit length ($\bar{c}_{perimeter}$ and $\bar{c}_{net}$). The quantities corresponding to a given thread (belonging to the net proper or to its perimeter) are considered in the calculation of both node masses and tension forces in simulation as per Eqs. (3) and (4). The stiffness, damping, and density properties are set to be the same for both the cable-based and LP-based nets. For the cable-based model only, the radius of the interior threads of the net and of the net perimeter are set as 0.0025 and 0.0035 m, respectively, to avoid a limitation imposed by the Vortex Studio framework and ensure proper collision detection of the target's thin geometries. Nonetheless, the linear density of the threads is kept the same as the experimental net, so that the total mass of the cable-based net is the same as that of the LP net and of the experimental net, of approx. 0.13 kg.

C. Determination of Number of Inner Nodes for the Lumped-Parameter Model

According to the LP model of the net, the mass of each thread or thread section is lumped into the nodes adjacent to it. By extension, in the model, threads (in the absence of inner nodes) or thread sections (in the presence of inner nodes) do not possess any collision geometry themselves. As a result, collisions can be represented only between the net and targets whose smallest size is larger than the distance between two adjacent nodes in the net.

For the mock-up Envisat target employed in the experiment of Ref. [26], the smallest dimension is $h_{panel} = 0.004$ m. To ensure that the modeled net can make contact with all of the parts of the target, it is therefore necessary that the distance between two adjacent nodes of the net is smaller than h_{panel}. This results in the following expression for the baseline number of inner nodes required for the realistic representation of the mock-up target capture in simulation [28]:

$$N_{I,\text{base}} = \left\lceil \frac{l_{\text{net},0}}{h_{\text{panel}}} \right\rceil - 1 \tag{6}$$

Table 2 Physical properties of the net

Parameter	Value
L_{side}, m	0.8
r_{net}, m	0.0005
$\bar{k}_{net}$, N	350
$l_{ct,0}$, m	0.14142
$r_{perimeter}$, m	0.0015
$\bar{k}_{perimeter}$, N	800
$l_{net,0}$, m	0.08
$\bar{\rho}_{net}$, kg/m	3.37E−04
$\bar{c}_{net}$, N · s	1.45E−04
m_{CM}, kg	0.03
$\bar{\rho}_{perimeter}$, kg/m	1.44E−03
$\bar{c}_{perimeter}$, N · s	1.45E−03

With $l_{\text{net},0} = 0.08$ m and $h_{\text{panel}} = 0.004$ m, it was determined that $N_{I,\text{base}} = 19$. However, to account for the fact that the relaxed distance joints permit slight increases in the distances between adjacent nodes, compared to the nominal length of a thread section, the value $N_{I,S} = N_{I,\text{base}} + 1 = 20$ is utilized for the validation. Next, $N_{\text{ct},S}$ is defined based on $l_{\text{ct},0}$ as

$$N_{\text{ct},S} = \left\lceil \frac{l_{\text{ct},0}}{l_{\min}} \right\rceil \tag{7}$$

As a result, for $N_{I,S} = 20$ and $l_{\min} = l_{\text{net},0}/(N_{I,S} + 1) = 0.00381$ m, it is determined that $N_{\text{ct},S} = 38$.

D. Determination of Initial Conditions

In addition to modeling the physical features of the experimental net and of the mock-up target, simulation of the experimental scenario also requires the modeling of launch (i.e., initial) conditions. This is not a trivial task, because the experimental net launch conditions are known only approximately.

Before the net is launched at the target, it is stored in a truncated-cone-shaped canister with $d_e = 0.107$ m. Complexity in recreating the initial conditions for the net launch is generated by the fact that the positions of the knots inside the ejector are not known. For the purpose of simulation, the net is assumed to be stored as a flat object with a side length of αL_{side}, where α is a constant—called *stowing ratio*—which defines the ratio between the initial side length of the net (in a stowed configuration) and the physical net side length. In an effort to match the experimental initial conditions, the value for α was chosen such that the initial square configuration of the net could be inscribed inside the circular ejector head. This can be enforced by the condition that the diagonal of the initial square configuration of the simulated net is equal to the diameter of the ejector head, leading to the following expression for the stowing ratio:

$$\alpha = \frac{d_e}{\sqrt{2} L_{\text{side}}} \tag{8}$$

Using Eq. (8), the stowing ratio is determined to be $\alpha = 0.094$ for the simulations conducted for this validation effort.

The initial configuration for the cable-based net is chosen such that its physical knots are in the same locations as those of the corresponding LP-based net. Unlike in the LP-based net (where the threads are simply represented by distance joints and nodes can be at distances smaller than the natural length of a thread), each cable in the cable-based net maintains a constant nominal length when not in tension. Thus, a zigzag pattern is used to arrange each cable so that the net can be "stored" (in modeling) in the same initial area as the LP-based net. This is achieved by constraining the cable to pass through five waypoints (labeled A_k to E_k for the kth cable and indicated in red in Fig. 4a) at the initial configuration. If the kth cable joins together node 1, k and node 2, k, the position vectors for the waypoints in the inertial reference frame are

$$\boldsymbol{r}_{A,k} = \boldsymbol{r}_{1,k} + a\hat{\boldsymbol{a}} + b\hat{\boldsymbol{b}} \tag{9a}$$

$$\boldsymbol{r}_{B,k} = \boldsymbol{r}_{1,k} + 2a\hat{\boldsymbol{a}} \tag{9b}$$

$$\boldsymbol{r}_{C,k} = \boldsymbol{r}_{1,k} + 3a\hat{\boldsymbol{a}} - b\hat{\boldsymbol{b}} \tag{9c}$$

$$\boldsymbol{r}_{D,k} = \boldsymbol{r}_{1,k} + 4a\hat{\boldsymbol{a}} \tag{9d}$$

$$\boldsymbol{r}_{E,k} = \boldsymbol{r}_{1,k} + 5a\hat{\boldsymbol{a}} - b\hat{\boldsymbol{b}} \tag{9e}$$

where $\boldsymbol{r}_{1,k}$ represents the inertial position of one of the physical knots of the net to which the cable is attached, and a, b, $\hat{\boldsymbol{a}}$, and $\hat{\boldsymbol{b}}$ are coefficients and unit vectors that are defined as

$$a = \frac{\alpha l_{\text{net},0}}{n_{\text{sec}}} \tag{10a}$$

$$b = \sqrt{\left(\frac{l_{\text{net},0}}{n_{\text{sec}}}\right)^2 - a^2} \tag{10b}$$

$$\hat{\boldsymbol{a}} = \frac{\boldsymbol{r}_{2,k} - \boldsymbol{r}_{1,k}}{\|\boldsymbol{r}_{2,k} - \boldsymbol{r}_{1,k}\|} \tag{10c}$$

$$\hat{\boldsymbol{b}} = -\hat{\boldsymbol{a}} \times \hat{\boldsymbol{k}} \tag{10d}$$

Figure 4b represents the resulting initial configuration of a net compressed with $\alpha = 0.094$, having 11 nodes on each side.

Additional complexity in recreating the initial conditions arises from the net launch velocities. Nominally, as prescribed in the experimental setup, the corner masses are launched with $v_e = 1.8$ m/s and $\theta = 25°$ [26]. However, actual launch speed and direction might differ from their prescribed values during the experiment, because of nonideal conditions. In principle, initial conditions for the simulation could be reconstructed from the experimental data. However, determination of accurate ejection velocities for the bullets in postprocessing of data is complicated by the fact that velocities were not recorded during the experiment, and that positional data are not available for every mass until more than 0.3 s after launch, due to reconstruction difficulties. For the sake of visualization, Fig. 5 reports the number of knots (out of the 121 total physical knots in the net) and of corner masses (out of 4) for which positional information is available during the experiment; for reference of the ideal situation,

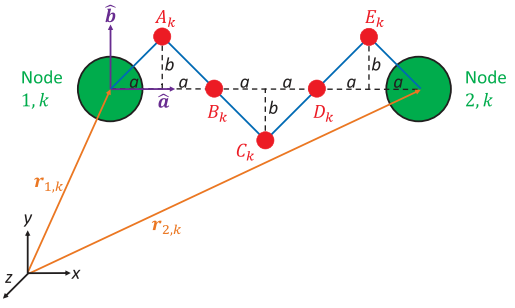

a) Waypoints configuration

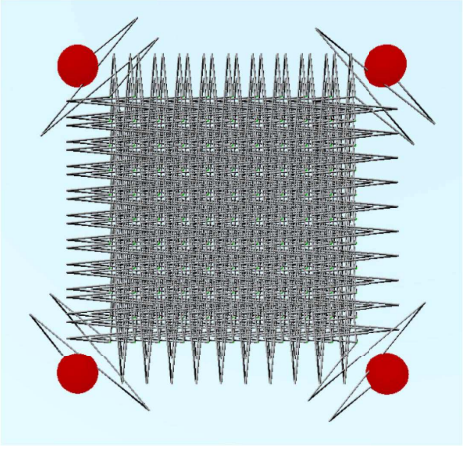

b) Stowed cable-based net

Fig. 4 a) Waypoints configuration and b) initial stowed configuration of the net with the cable-based model.

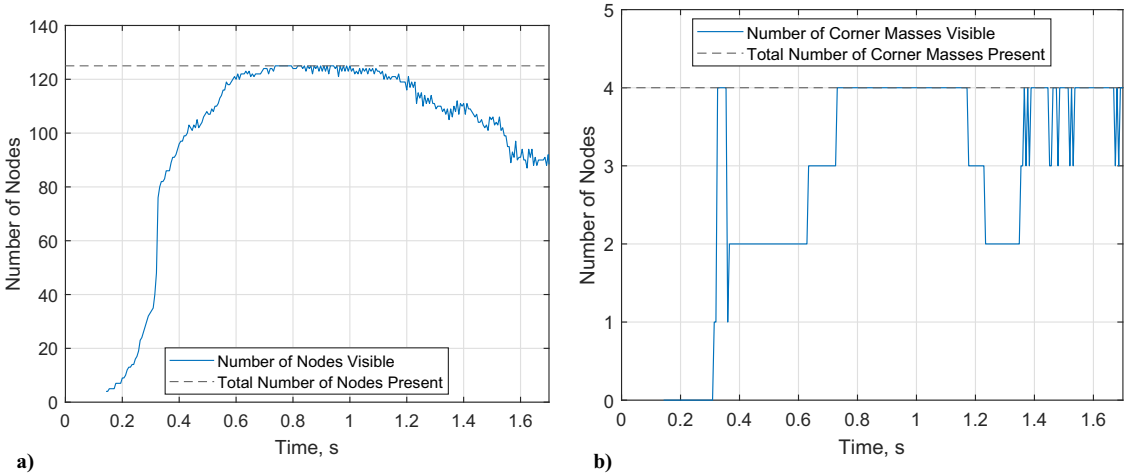

Fig. 5 Availability of positional information on nodes for a) the entire net (i.e., the physical knots and the corner masses), and b) the corner masses.

the total number of physical knots and that of corner masses present in the system are indicated with horizontal dashed lines. Because of these challenges, simulations were performed using the nominal values for the launch speed v_e and direction θ. The effect of uncertainties regarding these initial conditions on the validation effort will be briefly discussed in Sec. IV.A.

E. Collision Detection

In simulation, contact forces are calculated based on the overlap between the collision geometries of contacting bodies, as per the continuous compliant contact force modeling approach [20]. As a consequence of the small size of the net, of the tight initial stowing space, and of the choice of a planar stowing configuration in the modeling, the nodes of the LP net overlap in their initial positions. When $N_I = 20$, the central node has a diameter of 2.25 mm, while the surrounding inner nodes have diameters of 1.8 mm and have an initial center-to-center distance from the central node of 0.36 mm. Meanwhile, a knot located on the perimeter of the net has a diameter of 3.0 mm, while the surrounding inner nodes have a diameter of 2.9 mm. Because of the time needed for the motion of the corner masses to propagate to the center of the net, the distance between the central node and the closest inner nodes does not begin to increase until $t = 0.46$ s for the LP-based net. Similar issues arise with the initially overlapping cable sections of the cable-based model, as is clear from Fig. 4b.

Allowing collisions between nodes in the LP model and between cable sections in the cable-based model to happen before deployment has been achieved, and then, it would introduce unphysical forces into the simulation. To avoid such an issue, it is necessary that collision detection among nodes and cable sections is not performed during the deployment phase of the simulation, but only during the capture portion of the dynamics. The simulator at hand allows switching collision detection among the nodes and among the cable sections of the net on and off as desired, which proves to be useful in this instance.

F. Experimental Disturbances

Because of the parabolic flight environment, the net experienced residual gravity and Coriolis acceleration, which have considerable impact on the motion of the net [26]. Therefore, these must be included as external forces [see Eq. (2)] in the simulation for meaningful validation. On the other hand, consistent with previous validation works [8,11], aerodynamic drag force is assumed to be negligible. The resulting external forces acting on an individual node of the net can be expressed as

$$\boldsymbol{F}_{\text{par},i} = m_i \boldsymbol{g}_r - 2m_i(\boldsymbol{\omega}_r \times \boldsymbol{v}_i) \tag{11}$$

Values of $\boldsymbol{g}_r$ and $\boldsymbol{\omega}_r$ were recorded throughout the duration of the experiment [26] and were linearly interpolated in time for use in these simulations (a plot of the interpolated residual gravity and angular velocity versus time can be seen in Fig. 6). Then, forces due to the residual gravity and angular velocity are applied to every node in the net at each time step in the simulation, according to Eq. (11). The

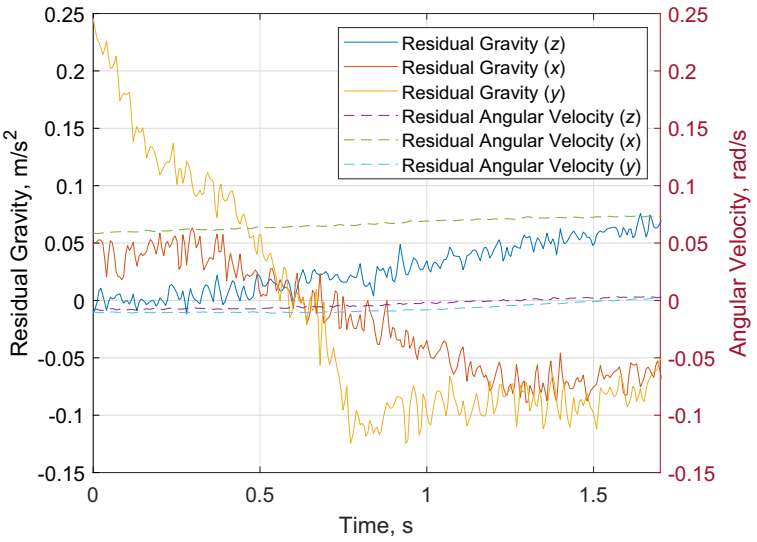

Fig. 6 Residual gravity and angular velocity experienced throughout the parabolic flight experiment.

same computation is made to apply the parabolic flight effects to the center of mass of each cable section in the cable-based net.

As it is clear from Fig. 6, the y direction is the direction in which the residual gravity has the most prominent effect on the motion of the net. From the same plot, it is also clear that the angular velocity of the aircraft is the greatest in the x direction, resulting in the Coriolis acceleration becoming most prominent in the y direction.

The effects of residual gravity, of Coriolis acceleration, and of both disturbances together on the y-direction motion of the central node of the net proper during simulation of the deployment phase can be seen in Fig. 7. Here, the results obtained with a LP model with no inner nodes, with an LP model with $N_I = 20$ and $N_{ct} = 38$, and with the cable-based model are reported. The LP model results are in accordance with Ref. [11], which provides confidence in both validation efforts.

IV. Validation Results

In this section, the simulator is validated by comparing its results to the available experimental data, employing both the cable-based modeling and the LP model with inner nodes. Analysis of the validation is separated into two distinct sections, concerning A) deployment dynamics, and B) capture dynamics. To gain insight into the effect that adding inner nodes along the threads of the net has on the behavior of the simulated net, and on the fitness of simulation to the experiment, results for deployment and capture are analyzed in the following for the cable-based net model and the LP models with four different values of N_I: $N_I = 0$ (corresponding to the traditional LP model), $N_I = 2$ (as a minimal case of including inner nodes), $N_I = 8$ (as an intermediate case), and $N_I = N_{I,S} = 20$ (i.e., the minimum number of inner nodes to represent collisions with all parts of the mock-up target, as was discussed in Sec. III.C). The number of nodes on each corner thread is $N_{ct} = 1$, 6, 16, and 38 for nets with $N_I = 0$, 2, 8, and 20, respectively. Throughout validation, the difficulties related to the availability of positional data and to the reconstruction of initial conditions (as per Sec. III.D) should be recalled.

A. Deployment Validation

Snapshots of the dynamics of the experimental net, of the net simulated utilizing the cable-based model with $n_{sec} = 6$, and of a simulated net with 20 inner nodes ($N_I = 20$) and 38 nodes on each corner thread ($N_{ct} = 38$) are shown in Fig. 8, which is intended to help the reader visualize the motion of the net throughout deployment, along with the pose of the Envisat model. In all snapshots, the experimental net is indicated in red, the net simulated with the cable-based model is shown in green, and the net simulated with the LP model with inner nodes is shown in black. Figures 8a, 8c, and 8e show a view in the direction of net launch, whereas Figs. 8b, 8d, and 8f show lateral views at corresponding times. It is important to note that —as was made evident with Fig. 5—not all nodes of the experimental net are visible to the cameras at all times. The scenario at the first time for which a significant number of nodes are visible to the cameras (i.e., 83 nodes out of 125) is represented in Figs. 8a and 8b. In these and the subsequent screenshots, all nodes for which experimental data exist are shown, and a thread is drawn between any two nodes that are adjacent to each other in the net, according to the connectivity table. Figures 8c and 8d show 119 nodes of the experimental net at $t = 0.57$ s, and Figs. 8e and 8f display the experimental net's full set of 125 nodes at $t = 0.85$ s, just before contact with the Envisat scale model. In all snapshots, the full simulated nets are also depicted, with nodes corresponding to the physical knots more visible, but also including all inner nodes and thread sections.

The deployment phase for both the LP and parabolic flight experiment nets lasts approximately 0.92 s; the cable-based net was found to impact the target slightly earlier, at $t = 0.85$ s. From Fig. 8, it can be seen that the trajectories of both the simulated LP model and cable-based model corner masses are very similar to those of the parabolic flight experiment corner masses, notwithstanding the uncertainty in the initial conditions. It is interesting to note that, in the early stages of the deployment, the LP simulated net took more time to expand in the x and y directions (see Fig. 8a) compared to the experimental net. The cable-based simulated net also expanded slower than the experimental net in the x and y directions, but still faster than the LP simulated net in the initial stages of the deployment, as can be appreciated in Fig. 8a. In Figs. 8c and 8d it can be seen that, mid-deployment, the two simulated nets are open in a very similar way in the x–y plane, but that the cable-based net flattened out sooner than the LP-based net, thus achieving a more similar shape to that of the experimental net. At $t = 0.85$ s (see Figs. 8e and 8f), the LP-based net is found to almost impact the target in its fully expanded and flattened out configuration —alike to the parabolic flight experiment net; therefore, it is expected that its behavior will be similar to the experimental net during target capture, although not identical. Conversely, at the time of impact with the target, the cable-based net is seen to have a less expanded shape, which suggests the possibility of more important differences in behavior during capture compared to the other two nets.

Displacements of the corner masses (i.e., nodes 122, 123, 124, and 125), of representative nodes on the edges of the net (i.e., nodes 6, 56, 66, and 116), and of more central nodes of the net (i.e., nodes 39, 59, 63, and 83) are plotted in Figs. 9–11. Within these plots, $(.)^{S,LP}$ represents data from the LP-based simulated net with $N_I = 20$, $(.)^{S,C}$ represents data from the cable-based simulated net, and $(.)^{E}$ represents data from the experimental net. As can be seen from the plots, the positions of the simulated nodes followed similar patterns to those of their experimental counterparts with

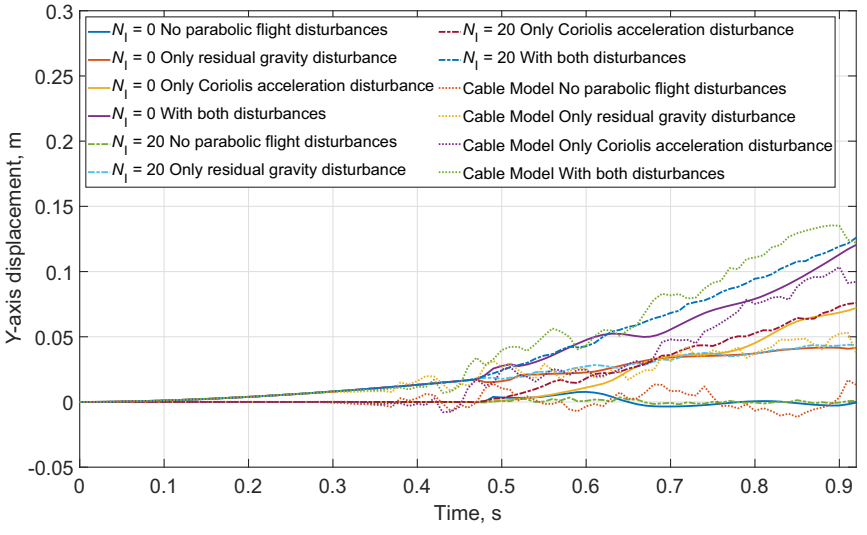

Fig. 7 Displacement of the central node of the net in the y direction during deployment, subject to varying disturbances.

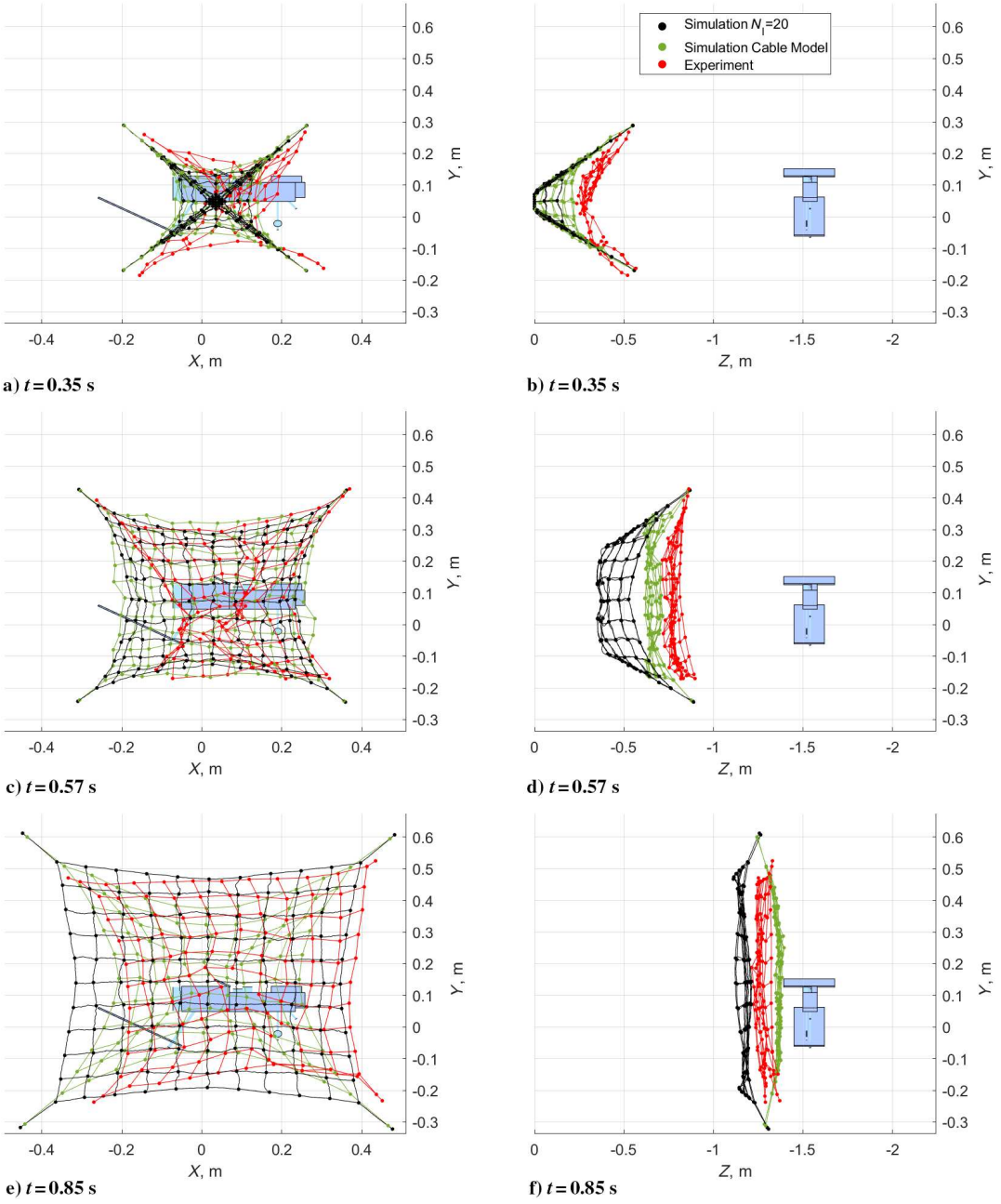

Fig. 8 Snapshots of experimental net, simulated LP net with $N_l = 20$, and cable-based model net during deployment.

both models. It can be noticed that, for the LP-based net, positional similarities between the simulated and experimental nodes are greatest for the corner masses, followed by the edge nodes; the central nodes exhibit the largest differences in terms of position. This reflects the behavior observed in Fig. 8, where the central area of the net lags behind the corner masses in the simulation. The results for the LP-based net with inner nodes compare favorably to results of the validation of an LP-based net *without* inner nodes by Shan et al. [11]. The results obtained with the cable-based model of the net show greater similarities to the experimental data: in fact, the trajectories of the corner masses of the cable-based net still align very well to those of their experimental counterparts in Fig. 9, and

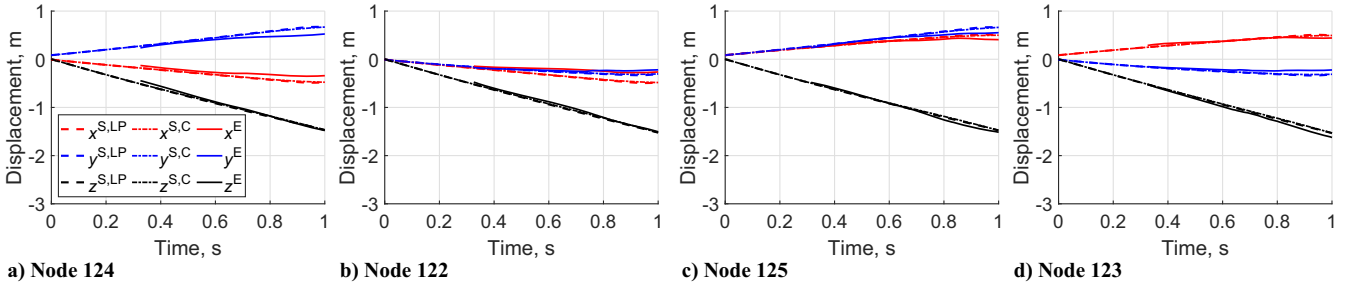

Fig. 9 Position of corner masses in time for the simulated and experimental nets.

the edge and central nodes of the cable-based net closely follow those of the experimental net in Figs. 10 and 11.

Another useful metric for validation is the residual error in the position of certain nodes during deployment, which can be calculated as the absolute error between the positions of a simulated ith knot and the corresponding experimental knot:

$$\boldsymbol{re}_i(t) = [|x_i^S(t) - x_i^E(t)|, |y_i^S(t) - y_i^E(t)|, |z_i^S(t) - z_i^E(t)|]^T \quad (12)$$

Figure 12 shows how the x, y, and z components of the residual error on node positions vary over time for the different models. The selected nodes are the third corner mass (i.e., node 124), the central knot of the net (i.e., node 61), and the central knot on the left edge of the net (i.e., node 56). Data from simulation with eight inner nodes are omitted from this plot for the sake of clarity and to avoid redundancy: trends with $N_I = 8$ were found to be very similar to the other LP cases with nonzero N_I. It should be noted that residual error for a given node can only be calculated when the position of the corresponding knot is available in the experimental data. It is for this reason that the comparison starts at different times for different nodes. The position of the knot corresponding to node 61, for instance, was only reconstructed starting 0.434 s after the launch of the net.

It can be seen that the motion of the third corner mass matches very closely in the simulation and the experiment. In fact, the residual error remains low—within 0.2 m—in all three directions for the duration of the deployment. Notable, however, is that the positions of the simulated and experimental bullets grow farther apart in the x and y directions as deployment progresses; because the trajectory of the bullet is largely defined by its initial velocity, this may be attributed to the uncertainty surrounding the exact initial conditions in the experiment.

The residual errors for the central node of the LP nets show a large discrepancy (of approx. 0.46 m) in the z direction when the experimental data first become available. Though the lack of experimental data for this node in the early stages of development makes the analysis difficult, this large error can be explained with the delayed movement of parts of the simulated LP net that are farther from the corner masses, relative to the experiment. In simulation, motion of the LP net is propagated along the threads from the corner masses, such that a node only experiences force when the distance between itself and an adjacent node is larger than the nominal length of the thread connecting them. In all LP simulated cases, node 61 does not begin moving until after $t = 0.46$ s; however, results of this comparison seem to indicate that the center of the net may have begun to move much sooner in the experiment. Notwithstanding the initial mismatch, the residual error in the z direction for the LP central node is very small (below approx. 0.01 m for all LP net) at the end of the deployment period. For the cable-based net, the residual error in the z direction for node 61 is much lower than for all LP-based nets (at 0.21 m) when the experimental data first become available; this indicates a more rapid propagation of the motion in early stages of deployment. The smallest residual in this direction is of 0.00064 m at $t = 0.62$ s; after this minimum, the error increases and remains at approx. 0.11 m until the net impacts the target, at $t = 0.85$ s. A similar pattern is seen with the knot on the left edge (i.e., node 56), which has a maximum residual error in the z direction of approximately 0.26 m and a final error of only 0.05 m for the LP case with no inner nodes. For the cable-based model, residual errors are smaller for most of the deployment; a minimum is seen around $t = 0.77$ s, and the error at $t = 0.85$ s is of approx. 0.1 m.

The residual errors in the x and y directions for node 56, with values below approximately 0.2 m, and for node 61, with values below approximately 0.12 m, remain smaller than the z-direction residual errors throughout most of the deployment. Increasing the number of inner nodes in the LP model is associated with lower residual errors in the z direction for node 61, and as the number of inner nodes is increased, this error begins decreasing sooner. A smaller, but noticeable improvement is also observed for node 56. On the other end, for the corner mass, increasing the number of inner nodes is not associated with any noticeable change in residual errors, as can be expected because the motion starts from the corner nodes.

For a statistical comparison, as well as to analyze the effect of including inner nodes in the model of the net, the root-mean-square error (RMSE) is computed between the data from the parabolic flight experiment and simulations, both on the overall position of the nodes of the net and on individual components of the position. The RMSE quantities of interest are computed as

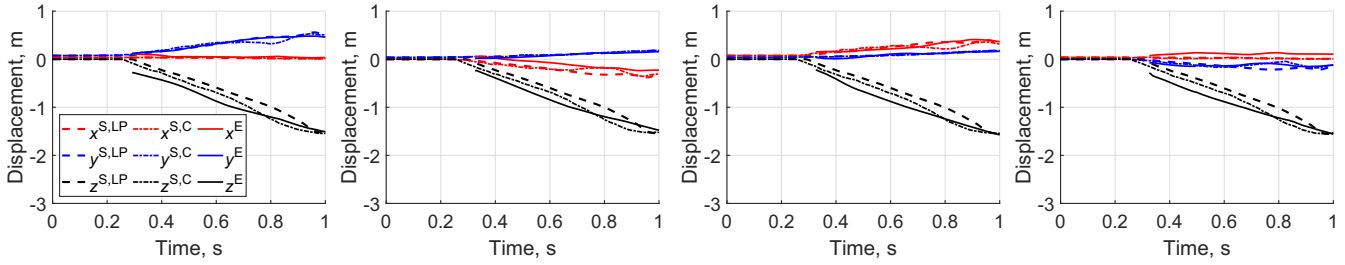

a) Node 116 b) Node 56 c) Node 66 d) Node 6

Fig. 10 Position of edge nodes in time for the simulated and experimental nets.

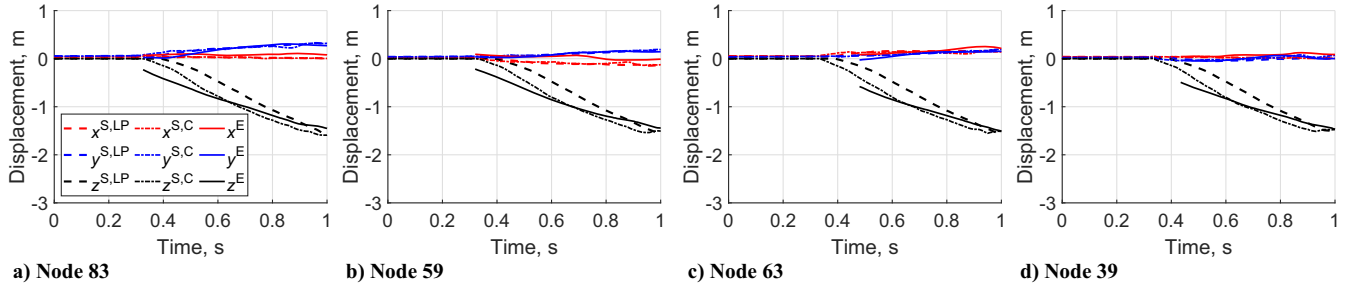

a) Node 83 b) Node 59 c) Node 63 d) Node 39

Fig. 11 Position of central nodes in time for the simulated and experimental nets.

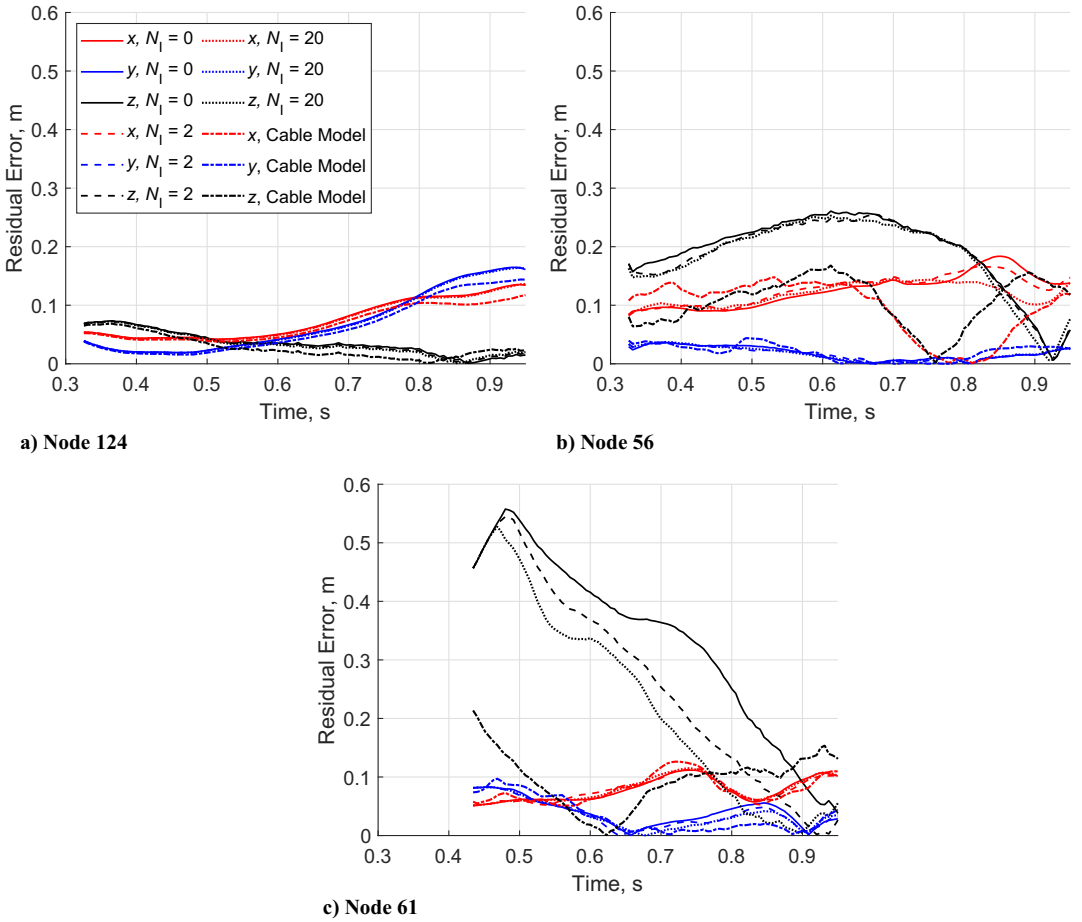

Fig. 12 The x, y, and z components of residual error on node positions over time with $N_I = 0$, $N_I = 2$, and $N_I = 20$, and with the cable-based model: a) for the third corner mass, i.e., node 124; b) for a knot on the edge, i.e., node 56; and c) for the central knot, i.e., node 61.

$$\mathrm{RMSE}_{\mathrm{total}}(t) = \sqrt{\sum_{i=1}^{N_{\mathrm{present}}(t)} \frac{(x_i^S(t) - x_i^E(t))^2 + (y_i^S(t) - y_i^E(t))^2 + (z_i^S(t) - z_i^E(t))^2}{N_{\mathrm{present}}(t)}} \tag{13}$$

$$\mathrm{RMSE}_x(t) = \sqrt{\sum_{i=1}^{N_{\mathrm{present}}(t)} \frac{(x_i^S(t) - x_i^E(t))^2}{N_{\mathrm{present}}(t)}} \tag{14}$$

$$\mathrm{RMSE}_y(t) = \sqrt{\sum_{i=1}^{N_{\mathrm{present}}(t)} \frac{(y_i^S(t) - y_i^E(t))^2}{N_{\mathrm{present}}(t)}} \tag{15}$$

$$\mathrm{RMSE}_z(t) = \sqrt{\sum_{i=1}^{N_{\mathrm{present}}(t)} \frac{(z_i^S(t) - z_i^E(t))^2}{N_{\mathrm{present}}(t)}} \tag{16}$$

Figure 13 reports the trends of the RMSE quantities in Eqs. (13–16) obtained with simulations with a varying number of inner nodes and with the cable-based model. Observing all plots, it can be seen that, at most times, using inner nodes in the simulation decreases the total RMSE between the positions of the nodes of the simulated LP and experimental nets. This indicates that—in addition to the expected improvement in capture performance—the introduction of inner nodes also improves the fitness of the deployment simulation to reality to some extent. Consistent with the trends noticed in Figs. 10 and 11, the error in the z coordinates is found to be the greatest out of the three coordinate axes at most time steps during the deployment. While the errors in the x and y coordinates reach maximum values of approx. 0.095 and 0.057 m, respectively, the error in the z coordinate is observed to be as high as 0.327 m (with $N_I = 0$) in the intermediate part of the deployment. Similar trends can be observed with other numbers of inner nodes. Out of all the simulated nets, the cable-based model yields the lowest RMSE values throughout most of the deployment duration. The maximum overall RMSE for the cable-based net is just 0.18 m, which is almost twice as small as the maximum overall RMSE for the LP net with $N_I = 20$. The total RMSE and the RMSE in the z coordinate for the cable-based net increased to greater values than those for the LP model only after approximately $t = 0.85$ s, when the cable-based net impacts the target, in advance of the experimental net. For both the RMSEs in the x and y coordinates, the values for the cable-based net are in general close to those of the LP-based nets, with slightly greater values between 0.3 and 0.5 s and slightly smaller values between 0.5 and 0.85 s.

Table 3 reports the averages of the RMSEs versus time. In accordance with Fig. 13, the error in the z coordinate is the greatest out of all coordinate axes for all of the simulated nets. As an example, with $N_I = 0$, the average RMSE for the z coordinates is approximately three times larger than the average RMSE of the x coordinate and more than five times larger than the average RMSE of the y coordinate. It is also confirmed that all average RMSE values during the deployment decrease with increasing values of N_I. Compared to $N_I = 0$, utilizing $N_I = 20$ decreases the total, x coordinate, y coordinate, and z coordinate average RMSE values by 11.02, 4.10, 11.92, and 12.39%, respectively. Consistent with trends observed in Fig. 13, the average total RMSE for the cable-based net is below that of all the LP-based nets. Compared with the LP model with $N_I = 20$, which is the best of the LP-based models, the total average RMSE for the cable-based net is almost 40% lower. A large improvement is also noticed in the average RMSE in the z coordinate axis, while in the x and y coordinate axes the improvements are less pronounced.

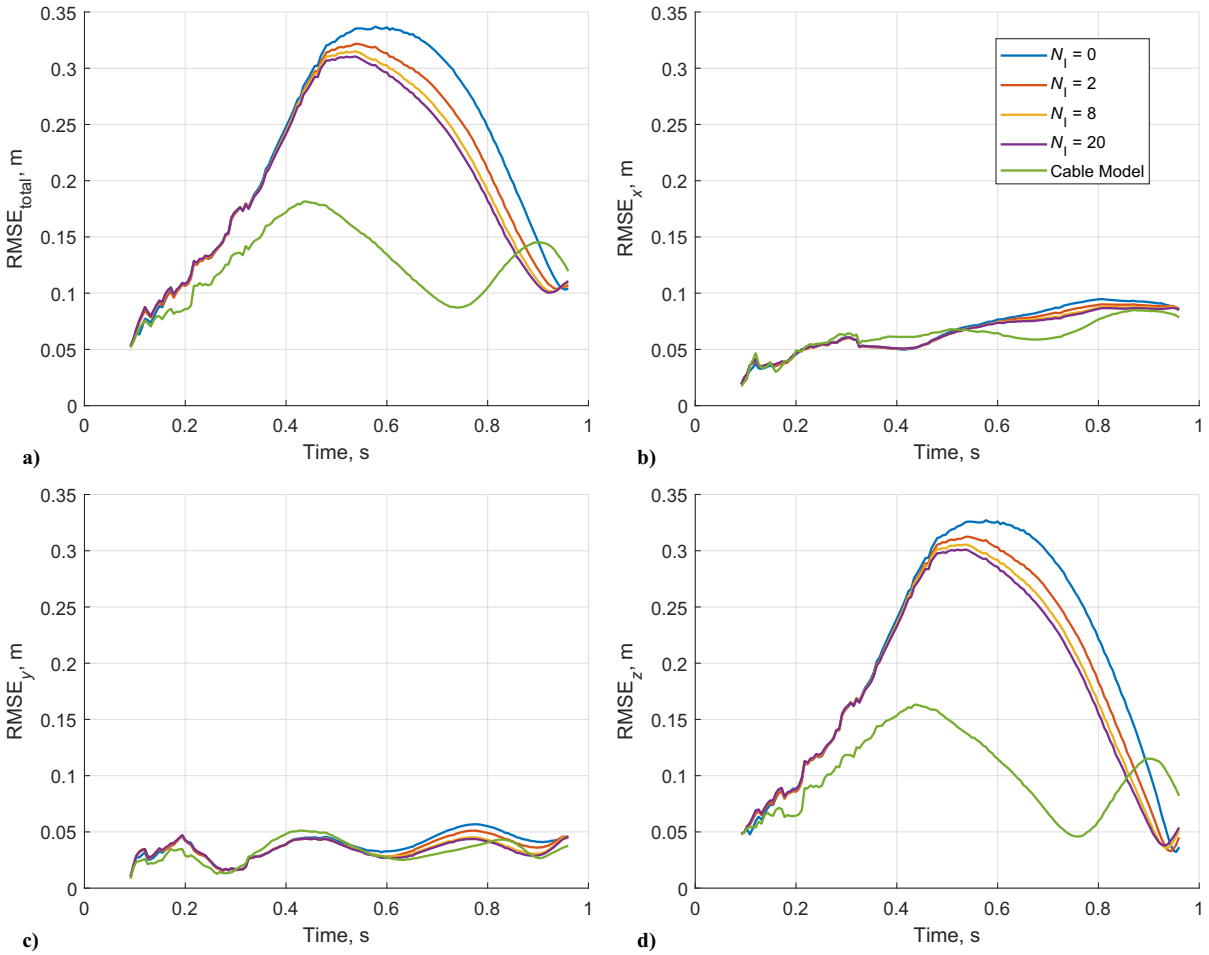

Fig. 13 RMSEs between experimental and simulation results for a) overall positions, b) x coordinates, c) y coordinates, and d) z coordinates, for different models of the net in simulations.

Table 3 Mean RMSEs during deployment for different models of the net

Mean RMSE	$N_I = 0$	$N_I = 2$	$N_I = 8$	$N_I = 20$	Cable model
$\text{RMSE}_{\text{mean,total}}$, m	0.2224	0.2080	0.2015	0.1979	0.1259
$\text{RMSE}_{\text{mean},x}$, m	0.0678	0.0624	0.0655	0.0650	0.0624
$\text{RMSE}_{\text{mean},y}$, m	0.0384	0.0361	0.0345	0.0339	0.0327
$\text{RMSE}_{\text{mean},z}$, m	0.2042	0.1892	0.1826	0.1789	0.1020

The tradeoff for employing the more precise LP model with inner nodes or the cable-based model is the increased computational time compared to the standard LP model (with $N_I = 0$). To integrate the dynamics of the net from its launch until the end of the deployment period, at $t = 0.92$ s, simulations with $N_I = 0$, $N_I = 2$, $N_I = 8$, and $N_I = 20$ took approximately 2.5, 3.5, 8.5, and 22 min, respectively, on a computer with Intel(R) Core(TM) i9-9900 CPU @ 3.10 GHz processor and GeForce GTX 1050 graphics card. This corresponds to almost a tenfold increase in the computational time from a deployment simulation with the standard LP model to one with the LP model with $N_{I,S} = 20$ inner nodes. On the same computer, simulation of the deployment with the cable-based model took 21 min to integrate, which is approximately the same time as for the LP net with $N_{I,S} = 20$ inner nodes. Here, it should be remembered that the deployment end time for the cable-based model is 0.85 s.

Overall, the results in this section validate the cable-based model and the inclusion of inner nodes in an LP-based model for the deployment dynamics of a net, within uncertainties in the initial conditions of the experiment. Analysis confirmed that finer discretization within the threads of the net improves the simulation fitness to reality, at the cost of increased computational time. The cable-based model yielded the best similarity with the experimental net, with computational cost similar to that of the most discretized LP-based net. Thus, the cable-based model presents itself as a promising alternative to the popular LP modeling, for the simulation of the deployment phase of net-based ADR.

B. Capture Validation

This section addresses the validation of the simulation of target capture for both the LP model and the cable-based model with the available experimental data. As was discussed in Sec. III.E, collisions between nodes in the LP-based net and between cable sections in the cable-based net are not modeled during deployment due to the unphysical effect that they would introduce to the simulation in its initial stages. These limitations are circumstantial and specific to the initial configuration of the net, such that contact between nodes of the net could, and should, be enabled during capture without unphysical effects on the dynamics. Modeling these forces—in addition to the forces of contacts between the net and the target—warrants consideration, as to do so is fundamentally more realistic. On the other hand, including collision detection among all nodes or cable sections—especially when several rigid bodies per thread are present—is bound to increase the computational cost notably. Therefore, an analysis of the effect of node-to-node and cable-to-cable collisions on capture dynamics is necessary.

First, the effect of modeling node-to-node collisions within the LP model on the dynamics of capture is analyzed by comparing two simulations where the net is modeled with eight inner nodes per thread, i.e., $N_I = 8$. In the first simulation, collisions among nodes are disabled throughout the whole deployment and capture, whereas in the second, collisions are enabled shortly before the initial contact of the net with the target (i.e., at $t = 0.92$ s). This is expected to determine

whether representation of contacts among parts of the net has an effect that justifies the increase in computational cost. Figure 14 displays 3D plots of the two simulated nets as contact with the target begins (i.e., at $t = 0.92$ s), as the net folds (at $t = 1.3$ s and $t = 1.5$ s), and at the end of the first wrapping period around the target (i.e., at $t = 1.7$ s). It is evident that the two nets (with and without collision detection among the nodes of the net) have exactly the same shape at $t = 0.92$ s, as is expected because the simulation conditions are exactly the same until this time. Later in the capture process, although the shape of the net does differ in the two simulations, it is observed that the general motion during initial wrapping is extremely similar: the nets fold around the target at similar rates and make contact with the target in similar ways. The shapes of the nets only diverge notably after they have fully enveloped the target; this is to be expected, because there are many more opportunities for the net to make contact with itself once it has completely wrapped around the target.

For a quantitative analysis of the effect of including node-to-node collisions during capture, Fig. 15a shows the total RMSE over the capture period between the two sets of simulation data, while Fig. 15b shows the RMSEs over time between each set of simulation data and

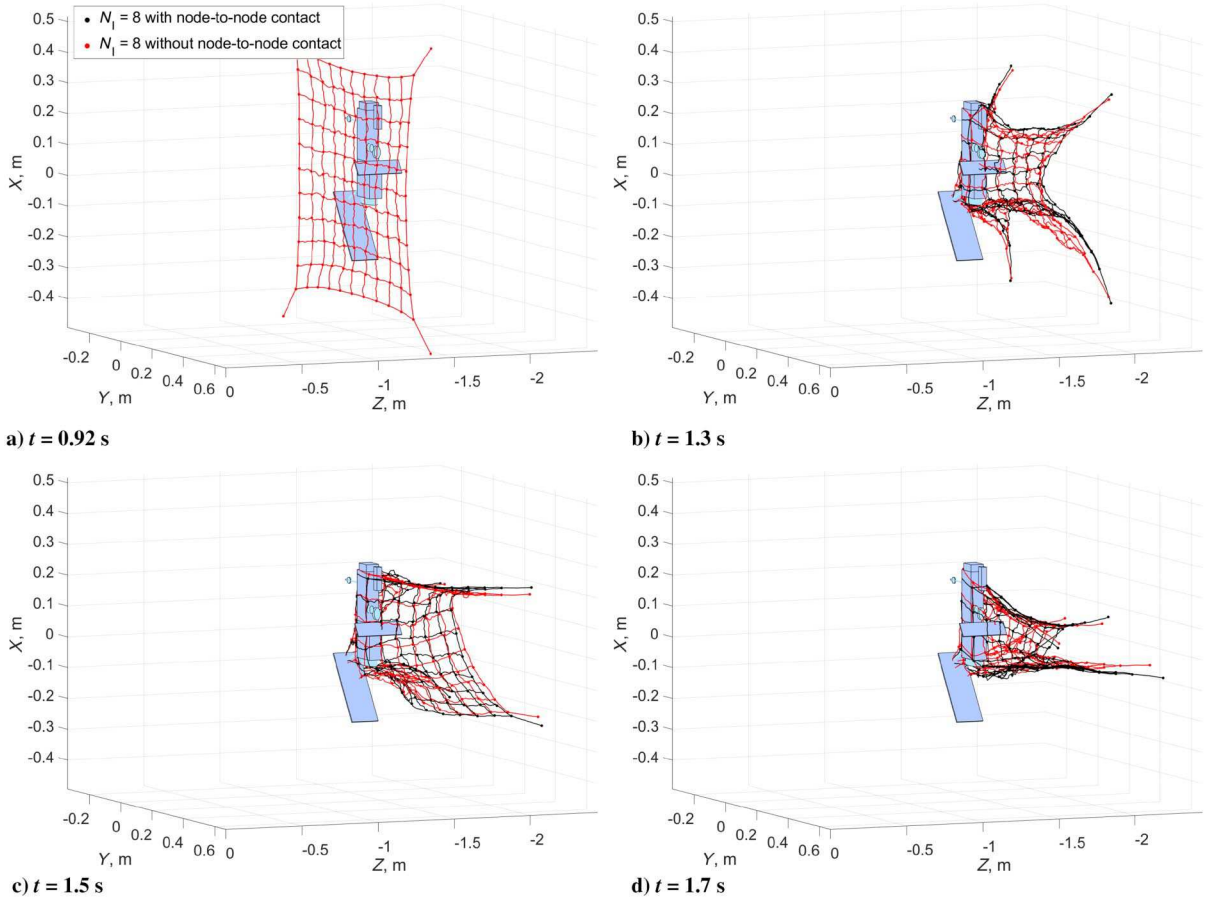

Fig. 14 Snapshots of simulated net with $N_I = 8$ during capture, with and without node-to-node collision detection.

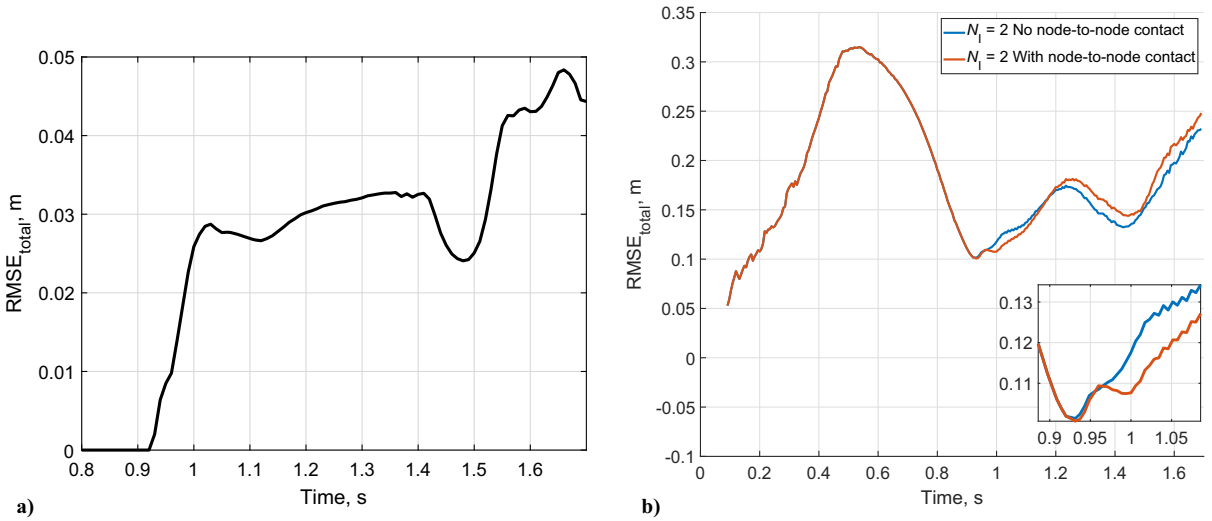

Fig. 15 RMSE of positions: a) between two simulated nets with $N_I = 8$, with and without node-to-node collision detection, and b) between the same simulated nets and the experimental data.

the experimental data. From Fig. 15a, it is confirmed that there are no numerical differences between the two sets of simulation data until $t = 0.92$ s. Moreover, it is observed that until the end of the first wrapping period (i.e., $t = 1.7$ s) the RMSE between the two simulations has a value lower than approximately 50 mm, which is small compared to the error between the simulated and experimental data, which is seen in Fig. 15b to be ∼0.24 m at $t = 1.7$ s. Figure 15b confirms that the discrepancy with the experimental results is exactly the same until 0.92 s; after this time, enabling collisions between nodes result in closer match to the experimental data up until $t = 1.17$ s. After $t = 1.17$ s, the simulation with no node-to-node collision yielded greater similarity with the experimental data. It should be noted that the limitations due to many knots in the experiment being not in the field of view of the cameras that recorded their positions (see Fig. 5) still affect this analysis.

Inclusion of collision detection and contact dynamics among nodes of the net was found to dramatically increase the computational time associated with simulation. With a time step of 0.0001 s, simulation with $N_I = 20$ and node-to-node collisions enabled during capture took more than 16 h to integrate 1.53 s of simulation on a computer with Intel(R) Core(TM) i9-9900 CPU @ 3.10 GHz processor and GeForce GTX 1050 graphics card, compared to approximately 7 h without node-to-node collisions. This increase in computational time becomes practically prohibitive later in the simulation, as the net wraps around the target and collisions between nodes happen more often. As an example, with contact among nodes enabled, just the hundredth of a second between 1.52 and 1.53 s took 45 min to simulate; the same simulation interval took just 3 min to integrate without modeling node-to-node contact.

The same analysis is performed for the cable-based model of the net. Similar to Fig. 14, Fig. 16 displays 3D plots of the two simulated cable-based nets right before contact with the target begins (i.e., at $t = 0.85$ s), as the net folds (at $t = 1.3$ s and $t = 1.5$ s), and at the end of the first wrapping period around the target (i.e., at $t = 1.7$ s). As expected, both nets have exactly the same shape at $t = 0.85$ s. As the wrapping of the target progresses, slight differences in the net shapes appear between the two simulations. Nonetheless, similarly to the comparison made with the LP-based net, the nets wrap around the target with comparable rates and form.

To quantitatively analyze the impact of including cable-to-cable collisions during capture, Figs. 17a and 17b display similar information to that of Figs. 15a and 15b for the cable-based net with and without cable-to-cable collisions. Comparing Fig. 17 with Fig. 15, it can be seen that both the difference with respect to the experiments and the difference between the cable-based nets with and without collision detection enabled between the threads are smaller than those of the LP-based nets, although of the same order of magnitude. Figure 17b indicates that the net with no cable-to-cable collision yielded a slightly smaller RMSE value from 1.4 to 1.6 s, but that results are otherwise very similar. As is expected, inclusion of cable-to-cable collisions increases the computational cost of the simulation compared to the case without it: integration of 1.7 s of the dynamics took 70 min with cable-to-cable collisions and 59 min without it. Although the difference is not as dramatic as for the LP-based net, the increase in computational time (of 18%) is still considerable.

Supported by the fact that node-to-node and cable-to-cable collision detection during the first target wrapping period does not have a critical effect on the simulated dynamics, the results discussed in the following refer to simulation considering only contacts between the net and the target. While other works have neglected the representation of collisions among parts of the net, this is—to the best of the authors' knowledge—the first time that the effect of neglecting thread-to-thread collision is evaluated to justify such a choice. As noted in work by Si et al. [13], tangling of the threads—enabled though self-collisions of the net—would become more important in later stages of target wrapping; however, later stages of capture are outside the scope of this work.

In the following, validation of capture in the following is based mainly on the visual representation of the shape of the wrapped net. In fact, i) the experimental data do not contain the positions of many knots during the capture period, and ii) it is not trivial to describe the

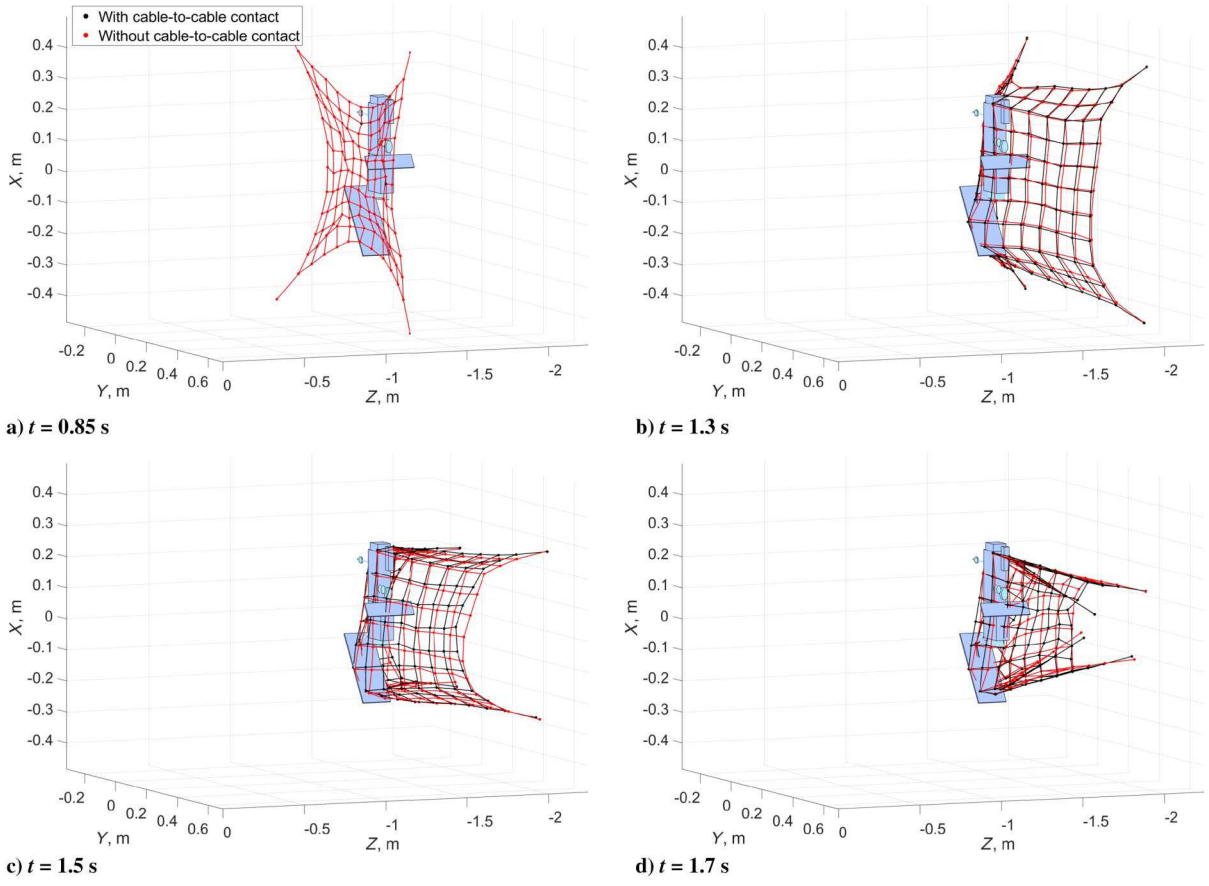

Fig. 16 Snapshots of cable-based simulated net during capture, with and without cable-to-cable collision detection.

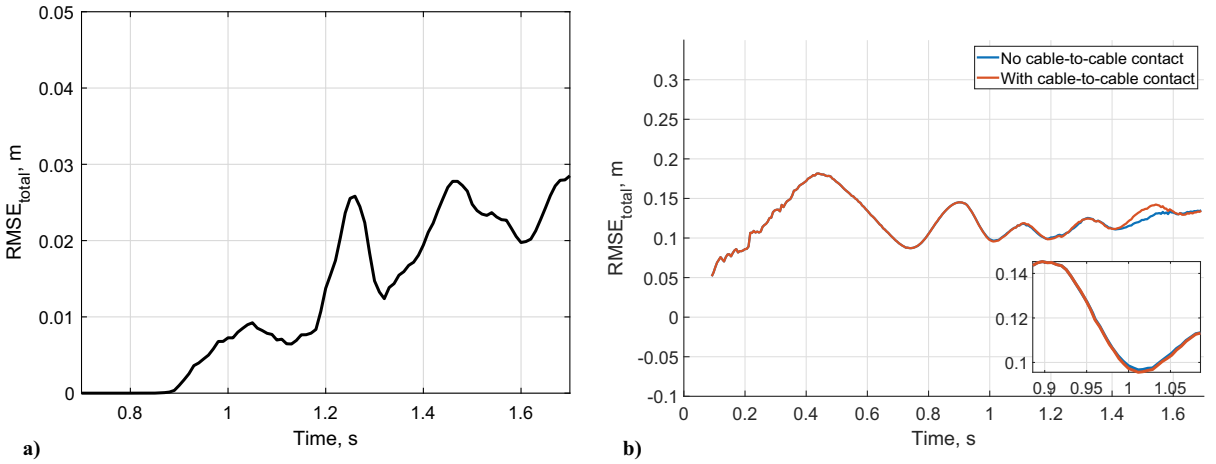

Fig. 17 RMSE of positions: a) between two cable-based simulated nets with and without cable-to-cable collision detection, and b) between the same simulated nets and the experimental data.

shape of a net during capture with quantitative measures. The simulation of capture dynamics is considered to be validated if the simulated cable-based net with $n_{\text{sec}} = 6$ and the simulated LP net with $N_{I,S} = 20$ show similar behavior to the experimental net during capture, and if both nets are able to represent all contacts with the parts of the Envisat model that the net wraps around.

The ability of a net with 20 inner nodes to capture the Envisat model is first of all confirmed visually in Fig. 18a, which shows a screenshot from the simulation graphics at time $t = 1.5$ s. Note the contact between the threads of the net and the solar panel model, i.e., the thin rectangular prism below the body of the model satellite. Taken at the same time step, the screenshot of the capture utilizing the cable-based model can also be seen in Fig. 18b.

Visual comparison of target capture in simulation with the LP-based net with $N_I = 20$, in simulation with the cable-based net, and in the experiment is provided in Fig. 19, both in the direction of net launch and from a lateral view. Snapshots at $t = 1.22$ s show the behavior of the nets shortly after they impacted the target; snapshots at $t = 1.43$ s are representative of an intermediate configuration of the three nets as they are wrapping around the target; finally, plots at $t = 1.70$ s illustrate how the first wrapping period of the three nets ends at approximately the same time. Close similarity between the shapes of the experimental and simulated nets can be observed throughout capture. The LP simulated and experimental nets envelop the target at approximately the same time and at approximately the same rate; this is also true for the cable-based net, even though its shape at the time of impact was different from the others (see Fig. 8). Additionally, all nets capture the main body and solar panel of the mock spacecraft, and the corner masses of the simulated nets swing around the body of the target in a similar pattern to those of the experimental net. One difference that can be noticed is that the thin vertical rod attached to the lower surface of the model does not appear to remain captured by the simulated nets at the end of the wrapping. This was investigated and was found to be due to the fact that this object passed through a mesh of the net when contact between the net and target first happened (see Fig. 8e), which represents a physically viable situation. Upon close inspection of the capture (see Fig. 20 for the LP-based net), it is confirmed that one of the threads did make contact with the rod attached below target body early on in the capture, at $t = 0.99$ s. However, due to the motion of the corner masses, after the initial collision the thread slid up the rod and remained on the lower surface of the target body for the rest of the simulation.

As was mentioned earlier, the inclusion of inner nodes to ensure proper collision detection comes at the cost of increased computational time, particularly during the capture phase, due to the increased number of contacts that need to be resolved. The number of net–target contact pairs—representing node–target pairs for the LP-based nets and cable section–target pairs for the cable-based net—at each time step is plotted for the cable-based net and the LP-based nets with $N_I = 0$, $N_I = 2$, $N_I = 8$, and $N_I = 20$ in Fig. 21. The number of net–target contact pairs for the net with 20 inner nodes is seen to exceed notably that of the other LP simulated nets: at $t = 1.7$ s, more than 500 contact pairs are detected, which is 5 times more than those for simulation with $N_I = 8$ and 10 times more than for $N_I = 2$. This increase is attributed to both the much larger number of nodes in the net itself, and to the ability of the net to capture thin geometries of the target, such as the solar panel. After initial wrapping of some portions of the target (i.e., the front and top sides), the number of contact pairs for the net with 20 inner nodes is observed to decrease notably from 1.25 to 1.42 s. This is explained by how the net initially envelops the top surface of the target body (see Fig. 19a), but is then momentarily lifted up from it due to the motion of the corner masses. By approximately $t = 1.43$ s, the net has fully wrapped around the solar panel as well as the lower right portions of the target body (see Fig. 19c), causing approx. 400 contacts between the net and the

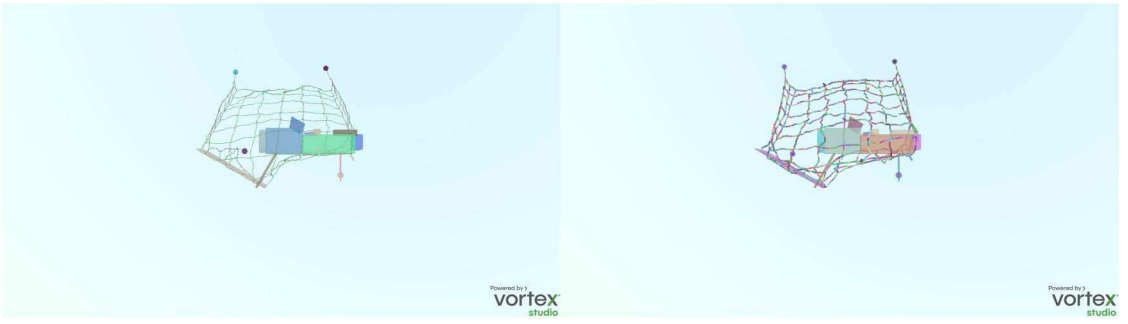

a) Lumped parameter with $N_I = 20$ **b) Cable-based model**

Fig. 18 Visual confirmation taken at $t = 1.50$ s of collision detection between net threads and smallest target geometry in simulation with a) $N_I = 20$ and b) cable-based model.

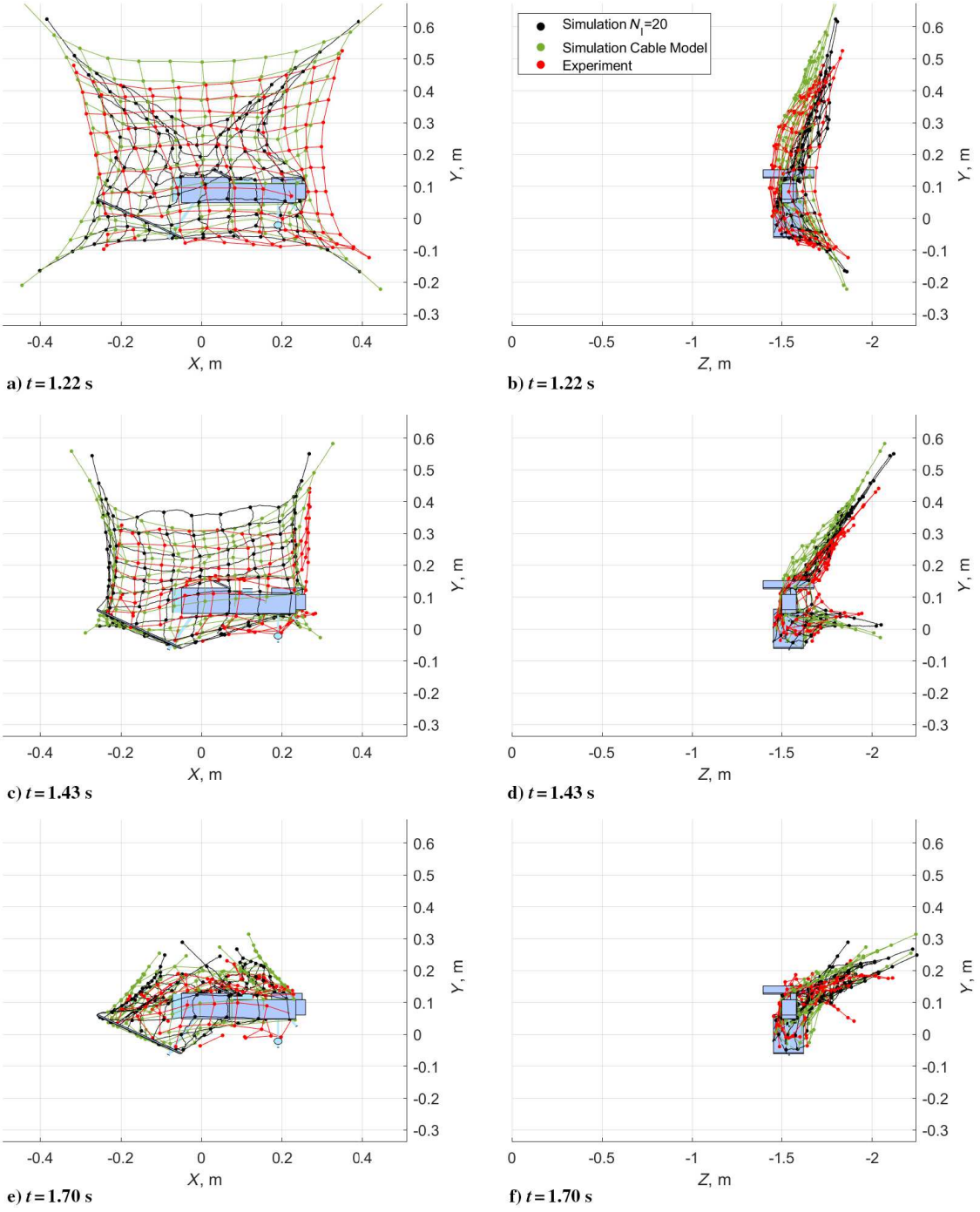

Fig. 19 Snapshots of experimental net, simulated LP net with $N_I = 20$, and the cable-based model net during capture.

target. As the net wraps around the back side of the target, the number of node–target contacts then continues to rise, to the maximum of approx. 500 at the end of the simulation. As a result of the different number of contact pairs in LP simulations with different numbers of inner nodes, the computational time for the capture period (i.e., from $t = 0.93$ s to $t = 1.70$ s) was found to be of approximately 2, 7, 20, and 179 min for $N_I = 0, N_I = 2, N_I = 8$, and $N_I = 20$, respectively (on a computer with Intel(R) Core(TM) i9-9900 CPU @ 3.10 GHz processor and GeForce GTX 1050 graphics card). Similar to the LP net with $N_I = 20$, the number of net–target contact pairs for the cable-based net rose throughout the capture; however, it remained contained, reaching 89 by the end of the simulation. On the same computer, simulation with the cable-based net took 38 min to integrate the entire capture period (i.e., from $t = 0.85$ s to $t = 1.70$ s). This demonstrates an important advantage of the cable-based model, which allows for the same collision detection ability as the $N_I = 20$ LP model while being approximately 4.7 times faster at integrating the capture dynamics.

To determine whether the capture of the target object by a net is successful and verify the quality of capture without the need for visual inspection, a numerical capture quality index (CQI) was proposed by Barnes and Botta [41]. This index can be leveraged here for further validation and analysis of the simulation results. The CQI is expressed as[§]

[§]Note that, because of the geometry of Envisat, the convex hull volume of the target was used to compute the CQI, differently from [41], where the volume of the target itself was used. This was obtained by extracting coordinates of the surface features of the target and using them as inputs of the *convhulln()* MATLAB function, which generates the convex hull of the target along with its volume.

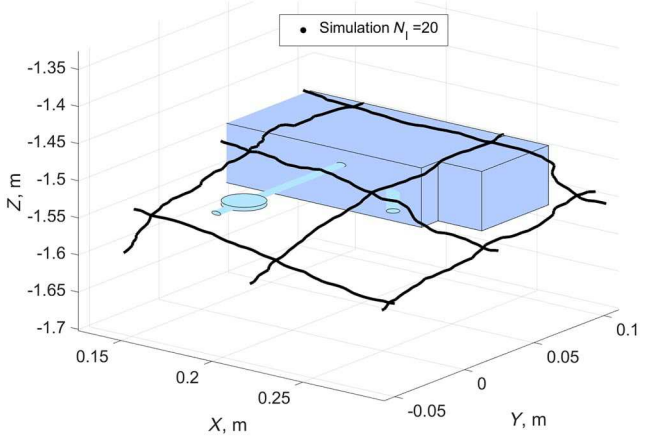

Fig. 20 Zoomed-in view of the target showing contact between the simulated net with $N_I = 20$ and thin rod attached below the target at $t = 0.99$ s.

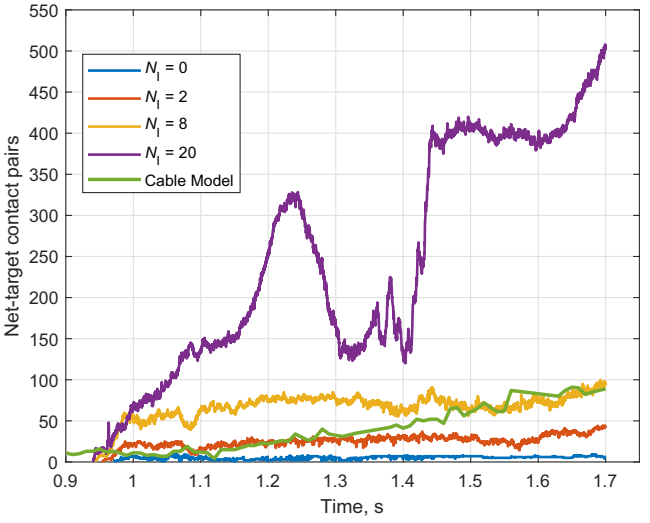

Fig. 21 Number of net–target contact pairs in time.

$$J = a_1 \frac{|V_n - V_t|}{V_t} + a_2 \frac{|S_n - S_t|}{S_t} + a_3 \frac{|q_n|}{L_c} \tag{17}$$

For the computation of the CQI, the corner thread inner nodes and the corner masses are omitted, as their positions do not affect the overall quality of capture. The weights a_1, a_2, and a_3 are dependent on the geometry of capture and taken here as 0.1, 0.1, and 0.8. To indicate that the capture of the target is successful, J must eventually converge toward a small constant value [41].

Figure 22 shows the CQI and its three components as a function of time for the LP simulated net with varying values of N_I and the cable-based net, along with corresponding values for the experimental net. Here, it should be noted that—because the computation of the CQI relies heavily on the nodal positions of the net—the CQI values of the experimental net may have limited accuracy at times when a large part of nodal position data is missing (e.g., for $t < 0.5$ s and $t > 1.5$ s). A gray scale is used to indicate the confidence in the experimental values of CQI, with higher number of nodes visible corresponding to higher confidence. Overall, it is observed that for the LP nets, the CQI terms follow similar trends, apart from the volume term (the difference in which stems from the differences seen during the deployment—see Figs. 8b and 8d). In Fig. 22a, it can be seen that the CQI decreases from a value of 31.0 at $t = 0$ to a value of approximately 2.7 for all LP simulated nets at $t = 0.98$ s; after that, the CQI value increases of non-negligible amounts for $N_I = 0$ and $N_I = 2$, and less for $N_I = 8$ and $N_I = 20$. Its final values at $t = 1.70$ s are of approx. 7.6, 6.4, 4.5, and 3.5 for $N_I = 0, 2, 8$, and 20, respectively. For the simulation with $N_I = 20$, a maximum value after net–target contact is reached at $t = 1.45$ s, before a small, gradual decrease; this trend can also be seen in the experimental net. The cable-based net follows all the curves of the experimental net very closely in shape. Compared to the LP nets, smaller values for the volume and surface area terms are observed from approx. $t = 0.4$ s to the end of deployment (see Figs. 22b and 22c), which is because the cable-based net has a more flattened-out geometry throughout most of the deployment, as seen in Figs. 8d and 8f. The cable-based net achieved a minimum CQI of 2.78 at $t = 0.92$. Resembling the $N_I = 20$ and experimental nets, a maximum value after net–target contact is reached at $t = 1.33$ s, before a slow decrease in value occurs.

The CQI values at the end of the capture phase for the experimental net, LP simulated net with $N_I = 20$, and the cable-based net were found to converge to a relatively small numerical value, of approx. 3, signifying successful capture. Overall, the trends of the CQI can signify successful capture with the simulated nets even without the need of visual inspection of the simulation graphics, and—together with the previously detailed analysis—indicate that both the simulation with LP $N_I = 20$ and cable-based nets are capable of replicating the experimental results with appreciable accuracy.

V. Conclusions

In this paper, efforts to validate a simulator for the deployment of nets and capture of space debris were presented. Models of the net with inner nodes along the threads and with flexible cable representation of threads were introduced to enable collision detection with the thin elements of the target employed in a parabolic flight experiment, modeled after the Envisat spacecraft. The experimental scenario was recreated in simulation, and the deployment and capture phases were analyzed, both qualitatively and quantitatively. Throughout this work, the effect of using flexible cables and a varying number of inner nodes along the threads was investigated in terms of accuracy of the simulation and of computational cost. The effect of modeling collisions among different parts of the net during deployment and capture was also evaluated for the first time.

Simulations were found to be in good agreement with experiments during the deployment of the net and the capture of the target, although with differences that are primarily due to the imperfect knowledge of launch conditions. Within the deployment phase, it was observed that the simulation fitness to reality was improved through the inclusion of higher numbers of inner nodes for the LP-based nets. Overall, the cable-based net showed greater similarity to the experimental net throughout deployment compared to the LP-based nets. It was demonstrated that both an LP-model with 20 inner nodes and a cable-based model can enable detection of collisions of the net with the thin geometries of the target, and improve notably capture realism compared to the traditional LP model for this experimental scenario; however, the cable-based model was found to be most computationally efficient. The effect of modeling thread-to-thread collision detection was determined to be negligible during deployment and the first target wrapping period.

As a result of this validation effort, there is confidence in the cable-based model of the net and in the LP model of the net with inner nodes, as well as in Hertzian contact mechanics, for the simulation of capture of targets with small geometries. Overall, increased confidence in the implemented simulator as a tool for studying and understanding the behavior of tether-nets in low-gravity environments is achieved. In future work, replicating behavior observed in an experiment where the target debris is rotating (instead of static) would provide a good validation opportunity for contact modeling, as more slipping between the net and the target surface would occur.

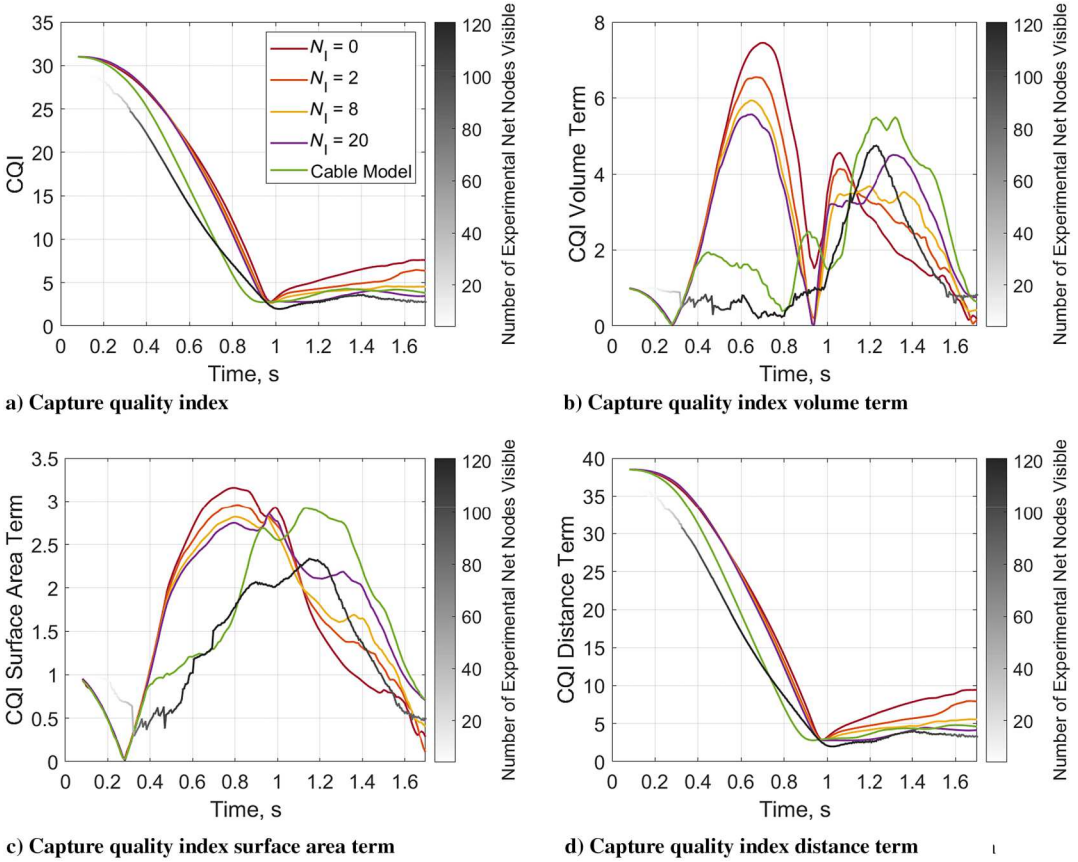

a) Capture quality index **b) Capture quality index volume term**

c) Capture quality index surface area term **d) Capture quality index distance term**

Fig. 22 Capture quality index and its individual terms for the experimental net and simulated nets with different numbers of inner nodes.

Acknowledgments

This work was funded by the National Science Foundation (NSF), under Civil Mechanical and Manufacturing Innovation (CMMI) Award No. 2128578. Any opinions, findings, and conclusions or recommendations expressed in this material are those of the author(s) and do not necessarily reflect the views of the National Science Foundation. Achira Boonrath acknowledges the University at Buffalo Presidential Fellowship. The authors would like to thank Wojciech Golebiowski, Kjetil Wormnes, SKA Polska, and ESA for providing data from the parabolic flight experiment and information about the experimental setup. The authors would like to thank CM Labs Simulations for providing licenses for the Vortex Studio simulation framework. Initial work by Rachael Gold and Cailean Woods is acknowledged.

References

[1] Anz-Meador, P., and Liou, J.-C., "Analysis and Consequences of the Iridium 33-Cosmos 2251 Collision," *38th COSPAR Scientific Assembly*, Committee on Space Research (COSPAR) Paper PEDAS1-0011-10, Bremen, Germany, July 2010.

[2] Wiedemann, C., Flegel, S., Möckel, M., Gelhaus, J., Braun, V., Kebschull, C., Kreisel, J., Metz, M., and Vörsmann, P., "Cost Estimation of Active Debris Removal," *63rd International Astronautical Congress*, International Astronautical Federation Paper IAC-12-A6.5.3, Naples, Italy, Oct. 2012.

[3] McKnight, D., Witner, R., Letizia, F., Lemmens, S., Anselmo, L., Pardini, C., Rossi, A., Kunstadter, C., Kawamoto, S., Aslanov, V., and Perez, J. C. D., "Identifying the 50 Statistically-Most-Concerning Derelict Objects in LEO," *Acta Astronautica*, Vol. 181, April 2021, pp. 282–291. https://doi.org/10.1016/j.actaastro.2021.01.021

[4] Ledkov, A., and Aslanov, V., "Review of Contact and Contactless Active Space Debris Removal Approaches," *Progress in Aerospace Sciences*, Vol. 134, Oct. 2022, Paper 100858. https://doi.org/10.1016/j.paerosci.2022.100858

[5] Botta, E. M., "Deployment and Capture Dynamics of Tether-Nets for Active Space Debris Removal," Ph.D. Thesis, McGill Univ., Montreal, 2017.

[6] Shan, M., Guo, J., and Gill, E., "A Review and Comparison of Active Space Debris Capturing and Removal Methods," *Progress in Aerospace Sciences*, Vol. 80, Jan. 2016, pp. 18–32. https://doi.org/10.1016/j.paerosci.2015.11.001

[7] Benvenuto, R., Salvi, S., and Lavagna, M., "Dynamics Analysis and GNC Design of Flexible Systems for Space Debris Active Removal," *Acta Astronautica*, Vol. 110, May 2015, pp. 247–265. https://doi.org/10.1016/j.actaastro.2015.01.014

[8] Medina, A., Cercós, L., Stefanescu, R. M., Benvenuto, R., Pesce, V., Marcon, M., Lavagna, M., González, I., López, N. R., and Wormnes, K., "Validation Results of Satellite Mock-Up Capturing Experiment Using Nets," *Acta Astronautica*, Vol. 134, May 2017, pp. 314–332. https://doi.org/10.1016/j.actaastro.2017.02.019

[9] Botta, E. M., Sharf, I., Misra, A. K., and Teichmann, M., "On the Simulation of Tether-Nets for Space Debris Capture with Vortex Dynamics," *Acta Astronautica*, Vol. 123, June 2016, pp. 91–102. https://doi.org/10.1016/j.actaastro.2016.02.012

[10] Botta, E. M., Sharf, I., and Misra, A. K., "Simulation of Tether-Nets for Capture of Space Debris and Small Asteroids," *Acta Astronautica*, Vol. 155, Feb. 2019, pp. 448–461. https://doi.org/10.1016/j.actaastro.2018.07.046

[11] Shan, M., Guo, J., Gill, E., and Gołębiowski, W., "Validation of Space Net Deployment Modeling Methods Using Parabolic Flight Experiment," *Journal of Guidance, Control, and Dynamics*, Vol. 40, No. 12, 2017, pp. 3319–3327. https://doi.org/10.2514/1.G002761

[12] Shan, M., Guo, J., and Gill, E., "Contact Dynamic Models of Space Debris Capturing Using a Net," *Acta Astronautica*, Vol. 158, May 2019, pp. 198–205. https://doi.org/10.1016/j.actaastro.2017.12.009

[13] Si, J., Pang, Z., Du, Z., and Cheng, C., "Dynamics Modeling and Simulation of Self-Collision of Tether-Net for Space Debris Removal," *Advances in Space Research*, Vol. 64, No. 9, 2019, pp. 1675–1687. https://doi.org/10.1016/j.asr.2019.08.006

[14] Endo, Y., Kojima, H., and Trivailo, P. M., "Study on Acceptable Offsets of Ejected Nets from Debris Center for Successful Capture of Debris,"

Advances in Space Research, Vol. 66, No. 2, 2020, pp. 450–461. https://doi.org/10.1016/j.asr.2020.04.012

[15] Huang, W., He, D., Li, Y., Zhang, D., Zou, H., Liu, H., Yang, W., Qin, L., and Fei, Q., "Nonlinear Dynamic Modeling of a Tether-Net System for Space Debris Capture," *Nonlinear Dynamics*, Vol. 110, No. 3, 2022, pp. 2297–2315. https://doi.org/10.1007/s11071-022-07718-7

[16] Huang, W., Zou, H., Liu, H., Yang, W., Gao, J., and Liu, Z., "Contact Dynamic Analysis of Tether-Net System for Space Debris Capture Using Incremental Potential Formulation," *Advances in Space Research*, Vol. 72, No. 6, 2023, pp. 2039–2050. https://doi.org/10.1016/j.asr.2023.05.054

[17] Hou, Y., Liu, C., Hu, H., Yang, W., and Shi, J., "Dynamic Computation of a Tether-Net System Capturing a Space Target via Discrete Elastic Rods and an Energy-Conserving Integrator," *Acta Astronautica*, Vol. 186, Sept. 2021, pp. 118–134. https://doi.org/10.1016/j.actaastro.2021.05.029

[18] Botta, E. M., Sharf, I., and Misra, A., "Evaluation of Net Capture of Space Debris in Multiple Mission Scenarios," *26th AAS/AIAA Space Flight Mechanics Meeting*, AAS Paper 16-254, Feb. 2016.

[19] Botta, E. M., Sharf, I., and Misra, A. K., "Energy and Momentum Analysis of the Deployment Dynamics of Nets in Space," *Acta Astronautica*, Vol. 140, Nov. 2017, pp. 554–564. https://doi.org/10.1016/j.actaastro.2017.09.003

[20] Botta, E. M., Sharf, I., and Misra, A. K., "Contact Dynamics Modeling and Simulation of Tether Nets for Space-Debris Capture," *Journal of Guidance, Control, and Dynamics*, Vol. 40, No. 1, 2017, pp. 110–123. https://doi.org/10.2514/1.G000677

[21] Shan, M., Guo, J., and Gill, E., "Deployment Dynamics of Tethered-Net for Space Debris Removal," *Acta Astronautica*, Vol. 132, March 2017, pp. 293–302. https://doi.org/10.1016/j.actaastro.2017.01.001

[22] Sharf, I., Thomsen, B., Botta, E. M., and Misra, A. K., "Experiments and Simulation of a Net Closing Mechanism for Tether-Net Capture of Space Debris," *Acta Astronautica*, Vol. 139, Oct. 2017, pp. 332–343. https://doi.org/10.1016/j.actaastro.2017.07.026

[23] Zeng, C., Hecht, G. R., Kumar, P. K., Shah, R. K., Botta, E. M., and Chowdhury, S., "Learning Robust Policies for Generalized Debris Capture with an Automated Tether-Net System," *AIAA Scitech 2022 Forum*, AIAA Paper 2022-2379, 2022. https://doi.org/10.2514/6.2022-2379

[24] Zhang, G., Zhang, Q., Feng, Z., Chen, Q., and Yang, T., "A Simplified Model for Fast Analysis of the Deployment Dynamics of Tethered-Net in Space," *Advances in Space Research*, Vol. 68, No. 4, 2021, pp. 1960–1974. https://doi.org/10.1016/j.asr.2021.04.032

[25] Shan, M., and Shi, L., "Analytical Method for Net Deployment Dynamics Modeling and its Experimental Validation," *Acta Astronautica*, Vol. 200, Nov. 2022, pp. 494–505. https://doi.org/10.1016/j.actaastro.2022.08.041

[26] Gołębiowski, W., Michalczyk, R., Dyrek, M., Battista, U., and Wormnes, K., "Validated Simulator for Space Debris Removal with Nets and Other Flexible Tethers Applications," *Acta Astronautica*, Vol. 129, Dec. 2016, pp. 229–240. https://doi.org/10.1016/j.actaastro.2016.08.037

[27] Gold, R., and Botta, E. M., "Validation of Simulation of Space Net Deployment Phase with Parabolic Flight Experiment Data," *AAS/AIAA Astrodynamics Specialist Conference*, American Astronautical Soc. Paper 19-783, Portland, Maine, Aug. 2019.

[28] Woods, C. T., Boonrath, A., Gold, R., and Botta, E. M., "Validation of Simulation of Space Net Deployment and Target Capture with Parabolic Flight Experiment Data," *AIAA Scitech 2022 Forum*, AIAA Paper 2022-1773, 2022. https://doi.org/10.2514/6.2022-1773

[29] Guang, Z., and Jing-rui, Z., "Space Tether Net System for Debris Capture and Removal," *2012 4th International Conference on Intelligent Human-Machine Systems and Cybernetics*, Vol. 1, IEEE, New York, 2012, pp. 257–261. https://doi.org/10.1109/IHMSC.2012.71

[30] Aglietti, G. S., Taylor, B., Fellowes, S., Ainley, S., Tye, D., Cox, C., Zarkesh, A., Mafficini, A., Vinkoff, N., Bashford, K., and Salmon, T., "RemoveDEBRIS: An In-Orbit Demonstration of Technologies for the Removal of Space Debris," *Aeronautical Journal*, Vol. 124, No. 1271, 2020, pp. 1–23. https://doi.org/10.1017/aer.2019.136

[31] Axthelm, R., Klotz, B., Retat, I., Schlossstein, U., Tritsch, W., and Vahsen, S., "Net Capture System for Debris Removal Demonstration Mission," *7th European Conference on Space Debris*, ESOC, Darmstadt, Germany, 2017.

[32] Lavagna, M., Armellin, R., Bombelli, A., Benvenuto, R., and Carta, R., "Debris Removal Mechanism Based on Tethered Nets," *11th International Symposium on Artificial Intelligence, Robotics and Automation in Space (i-SAIRAS 2012)*, European Space Agency, Turin, Italy, Sept. 2012.

[33] Wormnes, K., Jong, J. H. D., Krag, H., and Visentin, G., "Throw-Nets and Tethers for Robust Space Debris Capture," *Proceedings of the 64th International Astronautical Congress, IAC*, International Astronautical Federation, Paris, France, Sept. 2013, pp. 2260–2272.

[34] Chen, Q., and Yang, L., "On Dynamics of Casting a Net Structure of Flexible Cables on Orbit," *Proceedings of the 60th International Astronautical Congress, IAC*, International Astronautical Federation, Paris, France, Oct. 2009, pp. 5039–5044.

[35] Liu, H., Zhang, Q., Yang, L., and Zhu, Y., "Modeling and Simulation of Deployment Dynamics of Space Webs," *Proceedings of the 64th International Astronautical Congress, IAC*, International Astronautical Federation, Paris, France, Sept. 2013, pp. 2628–2635.

[36] Huang, C.-C., Tang, H.-J., and Liu, J.-Y., "Dynamical Analysis of Net Cage Structures for Marine Aquaculture: Numerical Simulation and Model Testing," *Aquacultural Engineering*, Vol. 35, No. 3, 2006, pp. 258–270. https://doi.org/10.1016/j.aquaeng.2006.03.003

[37] Takagi, T., Shimizu, T., Suzuki, K., Hiraishi, T., and Yamamoto, K., "Validity and Layout of "NaLA": A Net Configuration and Loading Analysis System," *Fisheries Research*, Vol. 66, Nos. 2–3, 2004, pp. 235–243. https://doi.org/10.1016/S0165-7836(03)00204-2

[38] Lee, C.-W., Lee, J.-H., Cha, B.-J., Kim, H.-Y., and Lee, J.-H., "Physical Modeling for Underwater Flexible Systems Dynamic Simulation," *Ocean Engineering*, Vol. 32, No. 3, 2005, pp. 331–347. https://doi.org/10.1016/j.oceaneng.2004.08.007

[39] Shan, M., Guo, J., and Gill, E., "An Analysis of the Flexibility Modeling of a Net for Space Debris Removal," *Advances in Space Research*, Vol. 65, No. 3, 2020, pp. 1083–1094. https://doi.org/10.1016/j.asr.2019.10.041

[40] Johnson, K. L., *Contact Mechanics*, Cambridge Univ. Press, Cambridge, England, U.K., 1987, Chap. 4: Normal Contact of Elastic Solid.-Hertz Theory.

[41] Barnes, C. M., and Botta, E. M., "A Quality Index for Net-Based Capture of Space Debris," *Acta Astronautica*, Vol. 176, Nov. 2020, pp. 455–463. https://doi.org/10.1016/j.actaastro.2020.06.044

C. Bonnal
Associate Editor